Water Resources Research

RESEARCH ARTICLE
10.1029/2018WR023517

Key Points:
- Realistic migrating ripples were analyzed for their hyporheic zone biogeochemical function
- The hyporheic zone nitrate removal efficiency increases asymptotically with Damköhler number
- Migrating ripples are less efficient in removing nitrate compared to stationary ripples

Supporting Information:
- Supporting Information S1
- Data Set S1

Correspondence to:
L. Zheng,
lizhizheng@utexas.edu

Citation:
Zheng, L., Cardenas, M. B., Wang, L., & Mohrig, D. (2019). Ripple effects: Bed form morphodynamics cascading into hyporheic zone biogeochemistry. *Water Resources Research*, *55*, 7320–7342. https://doi.org/10.1029/2018WR023517

Received 18 JUN 2018
Accepted 10 AUG 2019
Accepted article online 16 AUG 2019
Published online 29 AUG 2019

©2019. American Geophysical Union. All Rights Reserved.

Ripple Effects: Bed Form Morphodynamics Cascading Into Hyporheic Zone Biogeochemistry

Lizhi Zheng[1,2], M. Bayani Cardenas[1], Lichun Wang[1,3], and David Mohrig[1]

[1]Department of Geological Sciences, University of Texas at Austin, Austin, TX, USA, [2]Now at Tianjin Key Laboratory of Water Resources and Environment, Tianjin Normal University, Tianjin, China, [3]Now at Institute of Surface-Earth System Science, Tianjin University, Tianjin, China

Abstract The water quality and ecosystem health of river corridors depend on the biogeochemical processes occurring in the hyporheic zones (HZs) of the beds and banks of rivers. HZs in riverbeds often form because of bed forms. Despite widespread and persistent variation in river flow, how the discharge- and grain size-dependent geometry of bed forms and how bed form migration collectively and systematically affects hyporheic exchange flux, solute transport, and biogeochemical reaction rates are unknown. We investigated these linked processes through morphodynamically consistent multiphysics numerical simulation experiments. Several realistic ripple geometries based on bed form stability criteria using mean river flow velocity and median sediment grain size were designed. Ripple migration rates were estimated based primarily on the river velocity. The ripple geometries and migration rates were used to drive hyporheic flow and reactive transport models which quantified HZ nitrogen transformation. Results from fixed bed form simulations were compared with matching migrating bed form scenarios. We found that the turnover exchange due to ripple migration has a large impact on reactant supply and reaction rates. The nitrate removal efficiency increased asymptotically with Damköhler number for both mobile and immobile ripples, but the immobile ripple always had a higher nitrate removal efficiency. Since moving ripples remove less nitrogen, and may even be net nitrifying at times, consideration for bed form morphodynamics may therefore lead to reduction of model-based estimates of denitrification. The connection between nitrate removal efficiency and Damköhler number can be integrated into frameworks for quantifying transient, network-scale, HZ nitrate dynamics.

Plain Language Summary Sandy riverbeds are very rarely flat. They are typically covered by ripples and dunes. Because of their topography, these ripples and dunes drive variations in water pressure across their surfaces due to deflection, acceleration, and deceleration of the river flow. These pressure variations drive river water to infiltrate into the porous and permeable sediment where pressure is high and exit from the sediment where it is low. This pressure-driven flow, called hyporheic exchange, is critical to the water quality of rivers since it allows river water to undergo biogeochemical reactions that take place within the sediment. Ripples are highly dynamic however and respond readily to changes in river flow. How the migration and variable shape of ripples affect hyporheic exchange and the biogeochemical reactions it dictates is poorly understood and seldom studied. Here we bring concepts from ripple dynamics, river and groundwater hydraulics, and biogeochemistry into a unified modeling framework. The modeling was used to assess the effects of ripple migration on hyporheic zone biogeochemistry. We found that migrating ripples generally process less nitrate, a widespread pollutant, compared to their stationary counterparts. Thus, investigations and applications of hyporheic zone biogeochemical processes should pay attention to the dynamics of ripples.

1. Introduction

The global nitrogen cycle has been profoundly perturbed by human actions (Gruber & Galloway, 2008). This disruption has not only resulted in increasing amounts of nitrogen accumulated in ecosystems but has also enhanced the transformation within and transport of nitrogen between the biosphere, hydrosphere, and atmosphere (Galloway, 1998). Excess reactive nitrogen has caused serious ecological and environmental issues, including the degradation of water quality, coastal eutrophication, and dead zone formation (Craig et al., 2008), and loss of biodiversity (Birgand et al., 2007). Streambeds and riverbeds have been recently recognized as sites of nitrogen transformation due to biologically active sediment and steep redox

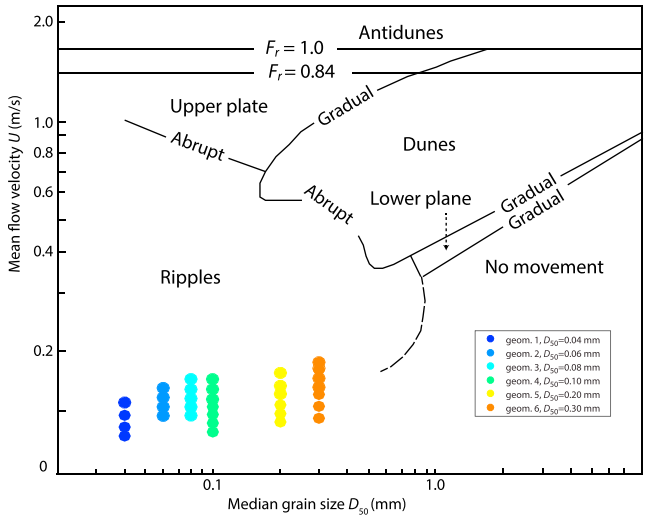

Figure 1. The bed form stability diagram (adapted from Ashley, 1990) showing the bed form geometry and hydraulic conditions considered in this study.

gradients (Bardini et al., 2012; Harvey et al., 2013; Marzadri et al., 2012; Zarnetske et al., 2012). Rivers and their sediment thus play an important role in controlling the fate of nitrogen, constraining its export to downstream waters that ultimately flow into the ocean (Alexander et al., 2000; Gomez et al., 2015; Kiel & Cardenas, 2014; Peterson et al., 2001).

River sediment commonly generates bed forms. Bed form morphology can strongly influence the spatial distribution of solute species and biogeochemical reaction zones within the sediment due to porewater exchange through the hyporheic zone (HZ; Buffington & Tonina, 2009; Cardenas et al., 2008; Harvey et al., 2012; Marzadri et al., 2012). Submerged bed forms in subcritical flows drive hyporheic exchange through two mechanisms: "pumping" and "turnover" (Elliott & Brooks, 1997b). Pumping is the interstitial movement of water through the streambed due to pressure gradients along the sediment-water interface which result from flowing water interacting with an irregularly shaped surface, that is, bed forms. Turnover occurs when a bed form migrates; as a bed form migrates, it captures water in the direction of migration along the bed form leeside and releases water from the stoss side. The contributions from these two mechanisms to hyporheic exchange flux have been well studied (Packman & Brooks, 2001).

Recent investigations have focused on denitrification in HZs to understand and predict the function of HZs in river corridor nitrogen cycling (Boano et al., 2014; Cardenas, 2015; Harvey & Gooseff, 2015; Hester et al., 2019; Malzone et al., 2016; Schmadel et al., 2016). In particular, studies have focused on whether HZs serve as a nitrate sink or source and on the factors that determine this (Boano et al., 2010; Kessler et al., 2015; Marzadri et al., 2012; Zarnetske et al., 2012; Zheng et al., 2016). However, most of the previous research has assumed that bed forms are immobile. Kessler et al. (2015) was a recent exception where they modeled hyporheic flow and reactive transport assuming a flat sediment-water interface but imposing on it a pressure distribution that would have resulted from the irregular topography of a ripple. This assumption effectively ignored the variable boundary conditions due to the movement of the bed form. For example, as a bed form migrates, water can also enter into the HZ from the leeside of the bed form. By assuming that the bed is flat, it ignored the part of the riverbed above bed form troughs, and this portion may be critical. That study missed or misrepresented turnover exchange. This could result in some errors in the kinematic structure of the shallow flow field, although these are expected to diminish with depth (Zlotnik et al., 2015). There may be larger errors in hyporheic exchange flux however, which may in turn affect solute transport and biogeochemical reactions close to the sediment-water interface.

Bed forms are naturally mobile during periods of sufficiently high river flow. Bed form movement can dramatically influence the hyporheic flow field (Ahmerkamp et al., 2015; Bottacin-Busolin & Marion, 2010), increase the exchange of solutes between streams and the hyporheic zone (Packman & Brooks, 2001), alter oxygen dynamics (Precht et al., 2004), produce an unwelcoming environment for benthic microorganisms (Rutherford et al., 1993), and influence organic matter retention, decomposition, and metabolism (Harvey et al., 2012). Thus, while bed form motion appears crucial for HZ hydraulics and biogeochemistry, it has mostly been ignored. The goal of this study is therefore to quantify hyporheic nitrogen cycling in mobile bed forms and to compare them with their immobile counterparts. We aim to determine how important bed form morphodynamics is and to analyze experiments across a parameter space designed for the development of predictive models. To our knowledge, this is the first systematic study of coupled hydraulic, biogeochemical, and morphodynamic processes of bed form-driven HZs. The analysis is done through experiments with multiphysics numerical models of a suite of single ripples.

2. Methodology

Ripples, whose wavelengths are typically <60 cm, and dunes, which are typically longer than 60 cm (Ashley, 1990), are the two most common types of bed forms in sandy rivers. Since ripple geometry is independent of water depth (García, 2008) and mainly controlled by mean sediment grain size, we only considered ripples in

this study for simplicity and as a starting point. Given a specific characteristic grain size, according to the bed form stability diagram (Figure 1), ripples represent the preferred or equilibrium bed configuration within a narrow range of stream velocities. This so-called equilibrium does not indicate a static bed form; in fact, the bed forms move and adjust their morphology while in a dynamic equilibrium. However, it can be assumed that the mean bed form geometry remains mostly unchanged if the stream velocity varies within a particular range. We used the bed form stability diagram (Figure 1) along with hydraulic criteria for ripple formation to establish ripple geometries. We considered six different mean grain sizes which translated directly to six different ripple geometries (Table S1 in the supporting information). Sediment grain size, assumed to be uniform and thus equal to D_{50}, is the only parameter that controls the ripple geometry following empirical equations (García, 2008; Raudkivi, 1997).

The mean stream velocity constrains the bed form formation and celerity. Thus, for each specific ripple geometry, we considered different stream velocities and its corresponding bed form celerity. We compared the hyporheic exchange flux, flow field, solute species spatial distribution, effective nitrification and denitrification reaction zone, and nitrate removal efficiency of mobile bed forms to their corresponding immobile bed forms.

2.1. Choice of Representative Bed Form Geometry: Ripples

The bed form stability diagram (Figure 1) is based on substantial field and experimental observations and covers all possible bed forms. In this study, we only considered two-dimensional ripples for simplicity since their shapes are controlled only by sediment size rather than flow depth. We used the bed form stability diagram together with the criterion for forming the bed form as discussed below to establish the experimental ripple geometries.

2.1.1. Criterion for Ripple Formation

The first constraint we followed is that only the space within the ripple domain in the bed form stability diagram is considered. On top of this, the experimental design obeyed several quantitative criteria as described below.

Two criteria for constraining bed form formation are generally based on the Froude number (F_r) or mean stream velocity U. The F_r, the ratio of inertial to gravitational force, is

$$F_r = \frac{U}{\sqrt{gH}} \tag{1}$$

where g is the gravitational acceleration and H is the flow depth. Since both dunes and ripples are characteristic of low subcritical flow regime, Karim (1995) proposed a bed form threshold predictor (F_t):

$$F_t = 2.716\left(\frac{H}{D_{50}}\right)^{-0.25} \tag{2}$$

where D_{50} is the mean sediment grain size. The F_t indicates the beginning of the transition regime which also marks the limit for subcritical flow; it therefore sets the limit for the existence of ripples and dunes. Dunes and ripples only exist if

$$F_r \leq F_t \tag{3}$$

Thus, H was chosen so that the condition in equation (3) is always met. Fixing $H = 0.1$ m, with depth referenced from the trough, satisfied equation (3) for all scenarios considered. This value was used for all simulations.

In addition to the above criterion, other studies (García, 2008; van Rijn, 1984b, 1993) showed that ripples are present when the dimensionless particle parameter $D^* < 10$ and the transport stage parameter $T < 3$ are both met. These metrics are calculated following:

$$D^* = D_{50}\left[\frac{Rg}{\nu^2}\right]^{1/3} < 10 \tag{4}$$

$$T = \frac{(u_*)^2 - (u_{*,cr})^2}{(u_{*,\mathrm{cr}})^2} < 3 \tag{5}$$

where $R = (\rho_s - \rho)/\rho$ is the submerged specific gravity of the sediment (1.65 for natural sediment), ρ_s is the density of the sediment grain, ρ is the density of water, ν is the kinematic viscosity of water, u_* is the shear velocity ($u_* = \sqrt{gHS}$, where H is the water depth and S is the slope of the stream), and $u_{*,cr}$ is the critical bed-shear velocity according to the Shields diagram (van Rijn, 1984a). u_* is determined by U. Further explanations can be found in García (2008) and van Rijn (1984b). U was chosen so that conditions in equations (4) and (5) were met.

Two additional criteria were considered: the existence of a viscous sublayer and the critical Shields stress. In particular, the corresponding thresholds are

$$R_p = \frac{u_* D}{\nu} \leq 11.6 \tag{6}$$

$$\tau_* > \tau_{*,cr} \text{ or } u_* > u_{*,cr} \tag{7}$$

In equation (6), u_* is the shear velocity and D is the grain size. In equation (7), τ_* is the Shields number ($\tau_* = \frac{u_*^2}{RgD_{50}}$), which characterizes sediment mobility, and $\tau_{*,cr}$ is the critical Shields parameter at entrainment, defined as $\tau_{*,cr} = \frac{\tau_{cr}}{g(\rho_s - \rho)D_{50}}$, and where τ_{cr} is the critical shear stress which is in turn related to the critical shear velocity ($u_{*,cr} = \sqrt{\frac{\tau_{cr}}{\rho}}$). The empirical Shields curve (a plot of $\tau_{*,cr}$ versus D^*) was used to estimate at what shear velocities sediment particles of a particular size will begin to move. We used the expression proposed by Soulsby and Whitehouse (1997) that describes the curve to calculate the threshold Shields parameter:

$$\tau_{*,cr} = \frac{0.30}{1 + 1.2D^*} + 0.055\left[1 - \exp\left(-0.02D^*\right)\right] \tag{8}$$

Satisfying the various criteria required an iterative workflow that was conducted manually (trial and error). The workflow is as follows:

1. Pick suitable grain sizes, that is, D_{50} (see below), which also established the ripple geometry (also see next section).
2. Conduct a simulation where streamflow was driven by a pressure drop (Δp) between the inlet and outlet. This pressure gradient corresponds to the slope S. Thus, only suitable values of S could be used since S is embedded in several of the criteria.
3. After a simulation with suitable S is conducted, the resulting corresponding U is calculated. This U is also used in the calculation for some criteria; thus, S was changed as needed if criteria with U in it (or derived from U) were violated. This includes staying within the ripple stability field in the bed form stability diagram.

Satisfying the multiple criteria led to a somewhat limited parameter space and number of cases. Many previous studies have considered more numerous cases, but our strict adherence to the criteria suggests that many cases in previous studies may not be realistic.

2.1.2. Determination of the Equilibrium Ripple Geometry

According to van Rijn's criterion for ripple formation ($D^* < 10$), ripples only develop in fine-grained sediments ($D_{50} < 0.4$ mm). We therefore chose six values of D_{50} ranging from 0.04 to 0.3 mm. Each D_{50} determines the wavelength and the height of ripples as described below, so we effectively investigated six ripples geometries (Figure 1). These geometries are referred to hereafter by their numbers (1–6, in increasing grain size) and/or their corresponding D_{50}.

Raudkivi (1997) proposed the following equations for ripple wavelength (L) and height (Δ) at the equilibrium state:

$$L = 75.4 \cdot \log(D_{50}) + 197 \tag{9}$$

$$\Delta = 3.4 \cdot \log(D_{50}) + 18 \tag{10}$$

where L, D_{50}, and Δ are all in millimeters. Bed forms under mean unidirectional flows are generally asymmetric, with a gentle stoss side facing upstream and a steeper leeside downstream. Here the leeside angle is chosen as 30° (Lefebvre et al., 2014).

For a given D_{50}, the ripple geometry is in a state of dynamic equilibrium and remains unchanged within the range of flow velocity (Figure 1). Taking our geometry 6 (D_{50} = 0.3 mm) as an example (Table S1), when the mean stream velocity U varies from 9 up to 17 cm/s, the ripple geometry remains more or less constant with L = 157 mm and Δ = 16 mm according to equations (9) and (10). Moreover, the stoss side angle for geometry 6 is 7.1°, with the crest shifted to the right (crest distance L_c = 129 mm), and the aspect ratio (L/Δ) is 9.71.

Combining the criteria for bed form formation and the bed form stability diagram, we chose 33 cases (Table S1 and Figure 1) that span different D_{50} and U. For example, we simulated six cases with incremental $U = 2$ cm/s within the range of 9–17 cm/s for geometry 6 (Figure 1). The increments were variable for each geometry by necessity due to irregular boundaries and ranges in the bed form stability diagram.

2.1.3. Calculation of Ripple Celerity

Coleman and Melville (1994) proposed the relationship between the celerity (c), Δ, and U for small ripples:

$$\frac{c}{\left[\left[u_* - u_{*cr}\right]\left[\tau_* - \tau_{*,cr}\right]\right]}\left(\Delta/D_{50} - 3.5\right)^{1.3} = 40 \tag{11}$$

Equation (11) indicates that c is generally smaller for larger Δ. Since Δ and $u_{*,cr}$ are both related to D_{50}, and u_* is related to U, c thus varied for each ripple geometry at each specific U (manifested by changing S). The estimated and imposed c are shown in Table S1.

2.2. Numerical Model Description

The chosen representative morphodynamic-hydraulic conditions were then used for multiphysics simulations of open channel flow, hyporheic flow, and hyporheic reactive transport for each single ripple. Channel water flow and porewater flow were sequentially coupled following the multiphysics computational fluid dynamics approach of Cardenas and Wilson (2007). In this framework, the turbulent flow field is first modeled independently of the subsurface model. The resulting pressure distribution along the sediment-water interface (SWI) from the turbulent flow model is then imposed as a Dirichlet boundary condition driving a porewater flow model of the HZ. The resultant groundwater velocity field is finally used as input for modeling multicomponent reactive transport. The key details of the models are described below.

2.2.1. Fluid Flow Models: Turbulent Flow and Darcy Flow

Steady state, two-dimensional, turbulent channel flow over the bed forms was simulated by numerically solving the Reynolds-averaged Navier-Stokes (RANS) equations. For an incompressible and homogeneous fluid, the RANS reads as

$$\frac{\partial U_i}{\partial x_i} = 0 \tag{12}$$

$$\rho U_j \frac{\partial U_i}{\partial x_j} = -\frac{\partial P}{\partial x_i} + \frac{\partial}{\partial x_j}\left(2\mu S_{ij} - \rho \overline{u_j' u_i'}\right) \tag{13}$$

where ρ and μ are the fluid density and dynamic viscosity, P is the time-averaged pressure, $i, j = 1, 2$ are the spatial indexed corresponding to x and y directions, U_i (i = 1,2) and u_i' (i = 1,2) are the time-averaged and instantaneous velocity components in x_i (i = 1,2) directions, and S_{ij} is the strain rate tensor defined as

$$S_{ij} = \frac{1}{2}\left(\frac{\partial U_i}{\partial x_j} + \frac{\partial U_j}{\partial x_i}\right) \tag{14}$$

The Reynolds stresses are related to the mean strain rates by

$$\tau_{ij} = -\overline{u_j' u_i'} = \nu_t\left(2S_{ij}\right) - \frac{2}{3}\delta_{ij}k \tag{15}$$

where ν_t is the kinematic eddy viscosity, δ_{ij} is the Kronecker delta, and k is the turbulent kinetic energy. We adopt the k- ω turbulence closure scheme with the eddy viscosity ν_t, the specific dissipation ω, the turbulence dissipation rate ε, and the closure coefficient β^* which are defined as

$$\nu_t = \frac{k}{\omega} \tag{16}$$

$$\omega = \frac{\varepsilon}{\beta^* k} \tag{17}$$

The steady state transport equations for k and ω are

$$\rho\frac{\partial\left(U_j k\right)}{\partial x_j} = \rho\tau_{ij}\frac{\partial U_i}{\partial x} - \beta^*\rho\omega k + \frac{\partial}{\partial x_j}\left[\left(\mu + \mu_t\sigma_k\right)\frac{\partial k}{\partial x_j}\right] \tag{18}$$

$$\rho\frac{\partial\left(U_j \omega\right)}{\partial x_j} = \alpha\frac{\rho\omega}{k}\tau_{ij}\frac{\partial U_i}{\partial x_j} - \beta\rho\omega^2 + \frac{\partial}{\partial x_j}\left[\left(\mu + \mu_t\sigma_\omega\right)\frac{\partial \omega}{\partial x_j}\right] \tag{19}$$

RANS-derived pressure distributions at the bottom of the turbulent flow domain (the SWI) obtained from the above equations were imposed as a boundary condition for the subsurface ripple domain.

The pressure field (or head field) in the HZ is calculated by solving the Laplace (or groundwater flow) equation:

$$\frac{\partial^2 h}{\partial x_i^2} = 0 \tag{20}$$

where h is the total hydraulic head. The velocity in the HZ can be estimated according to Darcy's law:

$$u_i = K\frac{\partial h}{\partial x_i} \tag{21}$$

where K is the hydraulic conductivity and u_i is the Darcy velocity in the i direction.

2.2.2. Representation of Bed Form Migration

Since we are investigating moving bed forms, we introduced a frame of reference moving at the bed form migration rate c to represent the effect of bed form celerity following Bottacin-Busolin and Marion (2010) and Kessler et al. (2015). In fact, this was originally proposed by Elliott and Brooks (1997a). One can also view this as a coordinate transformation of the horizontal coordinate, as how this approach was presented and implemented in Ahmerkamp et al. (2015). This approach works if the bed form maintains its shape as it migrates downstream at the rate c. The rate at which the leeside progrades horizontally is the same rate as the erosion of the stoss face. In this mobile bed form case, the horizontal porewater seepage velocity for the mobile bed form should have the bed form celerity c subtracted from it. This is possible because equation (20) is linear which allows for superposition. This is analogous to dragging the entire triangular mass of the bed form composed of porous and permeable sediment through a water column at speed c.

The celerity-corrected flow field, u_x-c, which now includes turnover, was further used as an input for solving the solute transport equations. The bed form migration has no effect on the vertical velocity. The porewater flow field is thus

$$\begin{cases} v_x = u_x/\theta - c \\ v_y = u_y/\theta \end{cases} \tag{22}$$

where θ is the sediment porosity and v_x and v_y are the average linear groundwater velocity.

2.2.3. Multicomponent Reactive Transport Model

The HZ is a hot spot for geochemical reactions partly due to the interaction of stream water and porewater in the sediment (Boulton et al., 1998; Fischer et al., 2005; Roley et al., 2012). We investigated and considered three major chemical reactions: aerobic respiration, denitrification, and nitrification. These are described by the following equations, respectively:

$$CH_2O + O_2 \rightarrow CO_2 + H_2O \tag{23}$$

$$5CH_2O + 4NO_3^- + 4H^+ \rightarrow 5CO_2 + 2N_2 + 7H_2O \tag{24}$$

$$NH_4^+ + 2O_2 \rightarrow NO_3^- + 2H^+ + H_2O \tag{25}$$

Thus, four reactive components are involved: dissolved organic carbon (DOC), dissolved oxygen (DO), nitrate (NO_3^-), and ammonium (NH_4^+). Other nitrate-relevant reactions are neglected.

The details of the sequential chemical reactions and associated reaction rates can be found in Zheng et al. (2016). Here we emphasize only the key features of the chemical reactions. The microbial degradation of DOC acts as the main source of energy, and therefore is assumed to be the primary reaction (Hunter et al., 1998). It follows the first-order rate law (Bardini et al., 2012):

$$r_{\mathrm{DOC}} = k_{\mathrm{DOC}} \cdot [\mathrm{DOC}] \tag{26}$$

where k_{DOC} is the first-order reaction rate constant; brackets indicate the actual activity of DOC rather than its concentration (but for our purposes these are interchangeable). The r_{DOC} is used to estimate the reaction rates for aerobic respiration (equation (23)). Aerobic respiration and nitrification are assumed to occur simultaneously, while denitrification (equation (24)) is only allowed to occur when the oxygen concentration dropped under a limiting value ([DO] < 1 mg/L). The electrons released by DOC oxidation are transferred to the potential terminal electron acceptors, first to O_2, and then to NO_3^- sequentially. The reduction rate of $r_{red,i}$ of the ith electron acceptor ($i = 1$ for O_2, $i = 2$ for NO_3^-) can be estimated by

$$r_{red,i} = f_i \cdot r_{DOC} \cdot \beta_i \tag{27}$$

where f_i is the fraction of electrons consumed by the ith reduction half-reaction and β_i is the ratio of the moles of transferred electrons per mole of oxidized DOC to the moles of electrons per mole of reduced compound in the ith reaction ($\beta_1 = 1$, $\beta_2 = 0.8$). The fraction f_i was defined with a simplified Monod formulation for the utilization of the terminal electron acceptors (Bardini et al., 2012; Hunter et al., 1998) following:

$$f_i = \left(1 - \sum_{n=0}^{i-1} f_n\right) \cdot \alpha_i \tag{28}$$

with $f_0 = 0$ and

$$\alpha_i = \begin{cases} \dfrac{C_i}{C_{i,lim}} & if\ C_i < C_{i,lim} \\ 1 & if\ C_i \geq C_{i,lim} \end{cases} \tag{29}$$

where C_i and $C_{i,lim}$ are the molar concentration and the molar limiting concentration of the ith reaction electron acceptor, respectively. α_i is a dimensionless parameter that allows for representing a limiting concentration ($C_{i,lim}$) for each electron acceptor.

Nitrification (equation (25)) followed a bimolecular rate law:

$$r_{NH_4^+} = k_{NH_4^+} \cdot \left[NH_4^+\right] \cdot [O_2] \tag{30}$$

where $k_{NH_4^+}$ is the nitrification molar rate coefficient.

The reaction kinetics above were employed to estimate the magnitude of the sink-source term (R) for simulating the fate of each component. At steady state, mass conservation is governed by the solute transport equation with R:

$$\nabla\cdot\left(-\theta D\nabla C_j + v\cdot C_j\right) = \theta R_j \tag{31}$$

where θ is the sediment porosity; j represents DOC, O_2, NO_3^-, and NH_4^+; D is the dispersion tensor; C_j is the concentration of component j; and v is the Darcy velocity. The NO_3^- from the river which enters the HZ and the NO_3^- internally produced from nitrification (and their products) were tracked as separate pools but combined when calculating overall reaction rates. This allowed for independent calculation of coupled (where the nitrification-produced NO_3 is being consumed) and decoupled (where the advected NO_3 from the stream is being consumed) denitrification.

For simplicity, we assumed that the HZ is initially free of any solutes including O_2 ($C_j = 0$). In-stream concentrations were assumed constant in time and space so these were specified as a Dirichlet boundary along portions of the SWI. The portions along the SWI where water exits out from the HZ were specified as an open boundary where no dispersive flux (zero concentration gradient) occurs at these boundaries.

Another simplification is we ignore sorption. Of all the solutes modeled, sorption is relevant primarily for ammonium (Triska et al., 1994). However, it has been shown that consideration for the sorption of ammonium does not provide additional insight with regards to overall HZ nitrogen cycling (Marzadri et al., 2011). Some streambeds have also been shown to exhibit minimal ammonium sorption (Butturini et al., 2000). Furthermore, we only considered steady state situations making sorption less relevant.

2.3. Calculation of Bulk Residence Time of Hyporheic Exchange

The residence time is the time it takes for a fluid or fluid-borne solute to enter from the stream, flow or be transported through the sediment, and eventually leave the sediment and return to the stream. At flow outlets, the mean residence time can be interchangeably used for age if the age = 0 at inflow sections of the SWI where stream water enters into the sediment (Goode, 1996). Note that residence time is different from flushing or turnover time (Monsen et al., 2002). Flushing time normally refers to the total or effective volume of a flowing body divided by the flow rate, which has been often used for HZ studies (Cardenas et al., 2008; Gomez et al., 2012).

To estimate the residence time for the HZ, we first solved the age-mass transport equation as presented by Goode (1996):

$$\frac{\partial(\theta\tau)}{\partial t} + \nabla\cdot(v\tau) = \nabla\cdot(\theta D\cdot\nabla\tau) \tag{32}$$

where θ is the sediment porosity and τ is the age mass. Solving equation (32) yields the field for τ which usually has a wide range especially at the SWI (e.g., Kaufman et al., 2017). However, none of the distributed τ along the SWI is representative of the HZ. Thus, like the traditional method used for estimating breakthrough curves from experiments and field surveys (Haggerty et al., 2002; Zarnetske et al., 2011), we applied the flux-weighted τ to estimate mean τ at the SWI; that is, the weighting coefficient for the distributed τ along the SWI is its associated local flux (normalized by the total flux) as determined from solving equations (20) and (21).

The mean τ at the SWI outlet, $\bar{\tau}_{out}$, which is also by definition the bulk residence time of the HZ, was used for estimating the Damköhler number (Da) in terms of DOC:

$$Da = \bar{\tau}_{out} k_{DOC} \tag{33}$$

Here Da is only relevant for reactions that involve or are connected to DOC. Since k_{DOC} is specified as constant as we implicitly assumed constant and uniform temperature, Da is thus proportional to the residence time. As such, a low Da most often represents a HZ with high D_{50} and thus high exchange flux.

2.4. Numerical Simulations With the COMSOL Multiphysics Finite Element Model

We solved the conservation equations above using COMSOL Multiphysics (COMSOL for short), a commercial finite element solver. These include solving the RANS equations to obtain pressure along the SWI, solving the Darcy's flow equation to yield Darcy velocity in the HZ at steady state, solving the steady state transport equations for calculating chemical reaction rate, and solving the age-mass equation to estimate mean residence time. The boundary conditions were the same as the previous study by Zheng et al. (2016). Turbulent open channel flow was modeled above a ripple bed form, the top boundary was a symmetry boundary, and the lateral boundaries were considered as a periodic boundary with a pressure drop (Δp) calculated based on the stream slope S (Bardini et al., 2012). The bottom of the surface domain was treated as a no-slip wall boundary ignoring the influence of the subsurface flow. For the multicomponent reactive transport model, the model domain was the single representative ripple. The top boundary of the porous sediment domain is a Dirichlet boundary corresponding to the RANS-derived pressure distribution. We assumed that all the nutrients and carbon in the HZ come from the stream water. Thus, the top boundary for the solute transport model had an open boundary condition. The lateral boundaries were also treated as spatially periodic boundaries with the same pressure drop as the open channel. The bottom of the porous sediment domain was treated as a no-flow/no-flux boundary in order to represent a neutral river (neither gaining nor losing net groundwater). The in-stream concentrations of the four reacting solutes considered are [DOC] = 150 mg/L, [DO] = 10 mg/L, $[NO_3^-]$ = 8 mg/L, and $[NH_4^+]$ = 1 mg/L, which represents a polluted or eutrophic stream case (Zheng et al., 2016). In our numerical experiments, we employed different permeability for different ripples as D_{50} changed (Table S1), but the same porosity = 0.37, longitudinal dispersivity = 3 cm, and transverse dispersivity = 0.3 cm were used for all cases. We used an empirical equation for permeability ($k = 7.35 \times 10^{-6} \times D_{50}{}^2$ (m^2) from Gangi (1985)).

In some of our previous similar multiphysics, multidomain modeling studies (Bardini et al., 2012; Cardenas & Wilson, 2007), the turbulent flow was modeled using a different numerical solver, but used COMSOL for modeling the subsurface domain. This approach has been shown to work well with COMSOL performing robustly in terms of modeling the HZ flow and transport field. Here however we used COMSOL to solve all equations, including the turbulent flow model. In light of this, we first tested whether COMSOL is sufficiently accurate and robust in reproducing the turbulent flow in the open channel by tuning the mixing length in the RANS turbulent flow module; section 3 first presents details of this test.

3. Results

3.1. Validation of Interfacial Pressure From Turbulent Flow Modeling With COMSOL

The simulated pressure distributions along the SWI were compared to the experimental measurements by Janssen et al. (2012) for validation. Following Janssen et al.'s experiment, six identical mean unidirectional current-type ripples with rounded troughs and crests and preceded and followed by 5-cm-long flat-bed sections were built in the model (Figure 2). Water depth was 10 cm above the bed form troughs. Two mean stream velocities that correspond to low-discharge (2.1 L/s) and high-discharge (3.6 L/s) flume experiments were simulated. The Janssen study instrumented a test ripple in the middle of a sequence of identical ripples; we focused on this test ripple.

We first compared the pressure along the top of a ripple from our COMSOL simulation with the measured pressure from the Janssen flume experiments (Figure 2). The overall patterns of the pressure distributions along the test ripple's SWI were mostly similar. The amplitude of the pressure variation across the bed form from our simulation was slightly larger in comparison with experimental measurements for both discharge cases. The relative errors were all within 10%. Additionally, we compared the velocity magnitude and the qualitative structure of the flow field which resulted from imposing the measured and simulated pressures at the SWI of the ripple (Figure 2). The magnitudes of porewater velocity were identical.

Since we are primarily concerned with HZ solute transport, we simulated the release of a conservative tracer to identify any differences in the solute propagation process (Figure 3). Our results showed that the size and shape of the plume using the simulated pressure fairly matched that of using the measured pressure, although the solute propagation front in the measured-pressure case was not as smooth as that in the

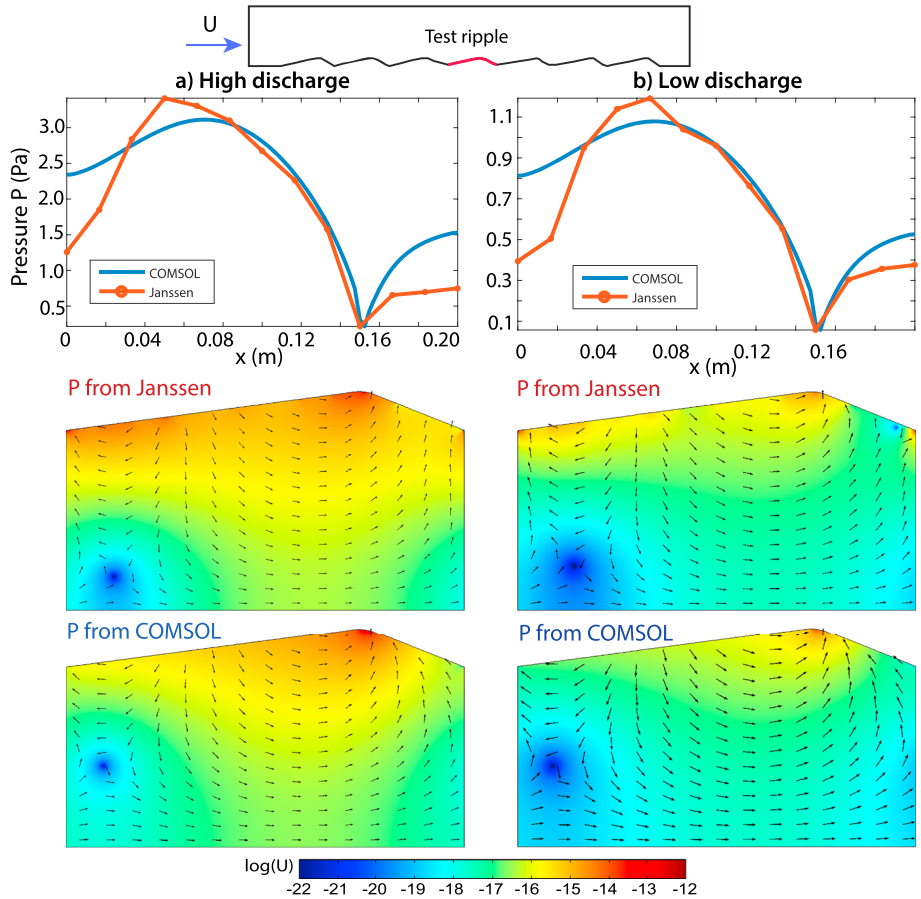

Figure 2. Comparison of hyporheic flow modeling results using pressure profiles along the sediment-water interface (top boundary) measured by Janssen et al. (2012) and using pressure modeled with COMSOL Multiphysics. Two channel discharge conditions following Janssen et al. are shown: (left) high and (right) low. The top row shows the pressure measured and modeled along the sediment-water interface for Janssen et al.'s test ripple.

COMSOL-modeled-pressure case. In summary, the difference in pressure between a COMSOL turbulent flow simulation and from experimental results led to subtle differences in flow and transport processes. This is well within the acceptable range for our purposes.

3.2. Turnover and Pumping Effects on the Flow Field and the Exchange Flux

The hyporheic flow boundary conditions change dramatically as a bed form starts migrating. There were stark and systematic differences between the mobile and immobile cases' flow fields and boundary conditions. For the finer grain size ($D_{50} < 0.08$ mm), all the mobile bed form cases have a higher exchange fluid flux than their immobile counterpart (Figure 4a and Table S2). For the coarse grain size ($D_{50} > 0.08$ mm), the immobile bed form has a higher exchange fluid flux as the migration rate is relatively small. As the migration rate becomes larger, the mobile bed form has higher exchange flux when turnover becomes dominant. This dominance is also reflected by the streamlines, which changed flow direction from left to right and became horizontal (Figure 4a and Table S2). The flux due to turnover in our study results in total hyporheic flux that can be orders of magnitude larger than pumping, which is the lone mechanism for the immobile bed form. Except for the smallest migration rate considered, all cases with migrating ripples showed that turnover is dominant and that exchange is thus simply due to the migration of the ripple. The hyporheic flow paths do not go deeper than the ripple trough and are all horizontal (see streamlines in Figures 5–8). On the other hand, the immobile bed form also shows a flow structure that does not change with stream velocity.

For the immobile bed form, there were two distinct hyporheic flow cells in the sediment (Figures 5–8). One was circulating clockwise (upstream), and the other was circulating counterclockwise (downstream); both of

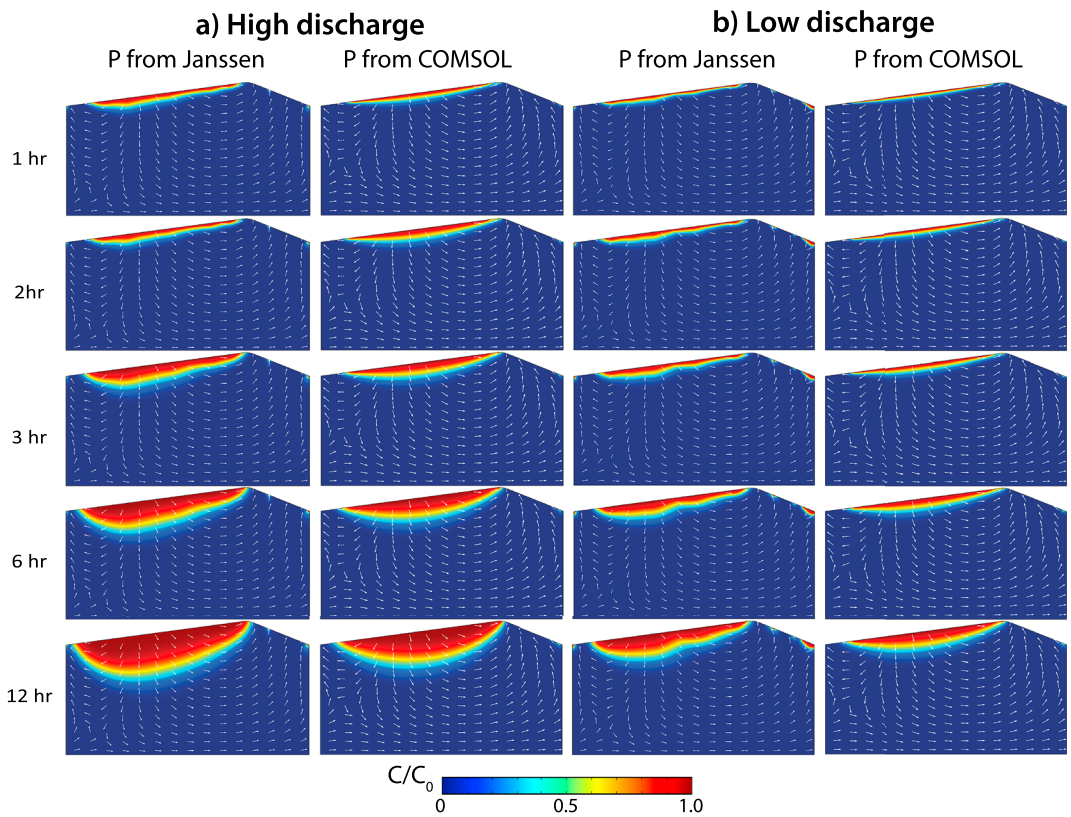

Figure 3. Comparison of snapshots of solute distribution from simulations using measured and COMSOL-modeled pressures cases corresponding to the high- and low-discharge experiments of Janssen et al. (2012).

these flow cells originate from the stoss side of the bed form. The streamlines show that underflow was from left to right. Solutes from the stream entered into the sediment through the middle part of the stoss side, and after a short flow path, exited the sediment through the leeside (some through the stoss side), and returned to the stream. This flow structure is typical for the pumping-only hyporheic exchange case.

The mobile bed form with the smallest ripple celerity (top row of Figures 5–8), where pumping and turnover exchange are both evident, had one more additional hyporheic flow cell. The additional flow cell originates from the right part and leeside of the ripple, and returns to the SWI at the crest. The general direction of underflow was from right to left, opposite to that in the immobile bed form. The average or dominant underflow direction reversed to right from left even at the smallest stream velocity and bed form celerity due to small velocities induced by pumping.

3.3. Comparison of Solute Distributions Between Mobile and Immobile Ripples

Since the geometry 6 (D_{50} = 0.3 mm) cases covered a relatively larger stream velocity variation range compared to other geometry cases, we focused on it to scrutinize the reactive solute transport processes and how these are affected by bed form migration. The distribution of DOC, DO, NO_3^-, and NH_4^+ across increasing U and corresponding c were analyzed (Figures 5 and 6).

Except for the smallest c cases, all mobile bed forms had flow fields dominated by turnover where fluid and solutes are simply translated from right (leeside) to left (stoss side) of the ripple. This makes the solute distribution almost uniform—the solutes entering the HZ, since it is translated across the actively migrating ripple, flushes, or inundates the entire ripple. Beneath the ripple (lower than the trough), the solutes resemble more a uniformly and vertically dispersing front that diminishes with depth. The transport beneath the ripple becomes limited by transverse dispersion. Bear in mind that the solutes here are reactive, so a conservative solute could penetrate deeper. The immobile bed forms show a progressive deepening of the solute

10.1029/2018WR023517

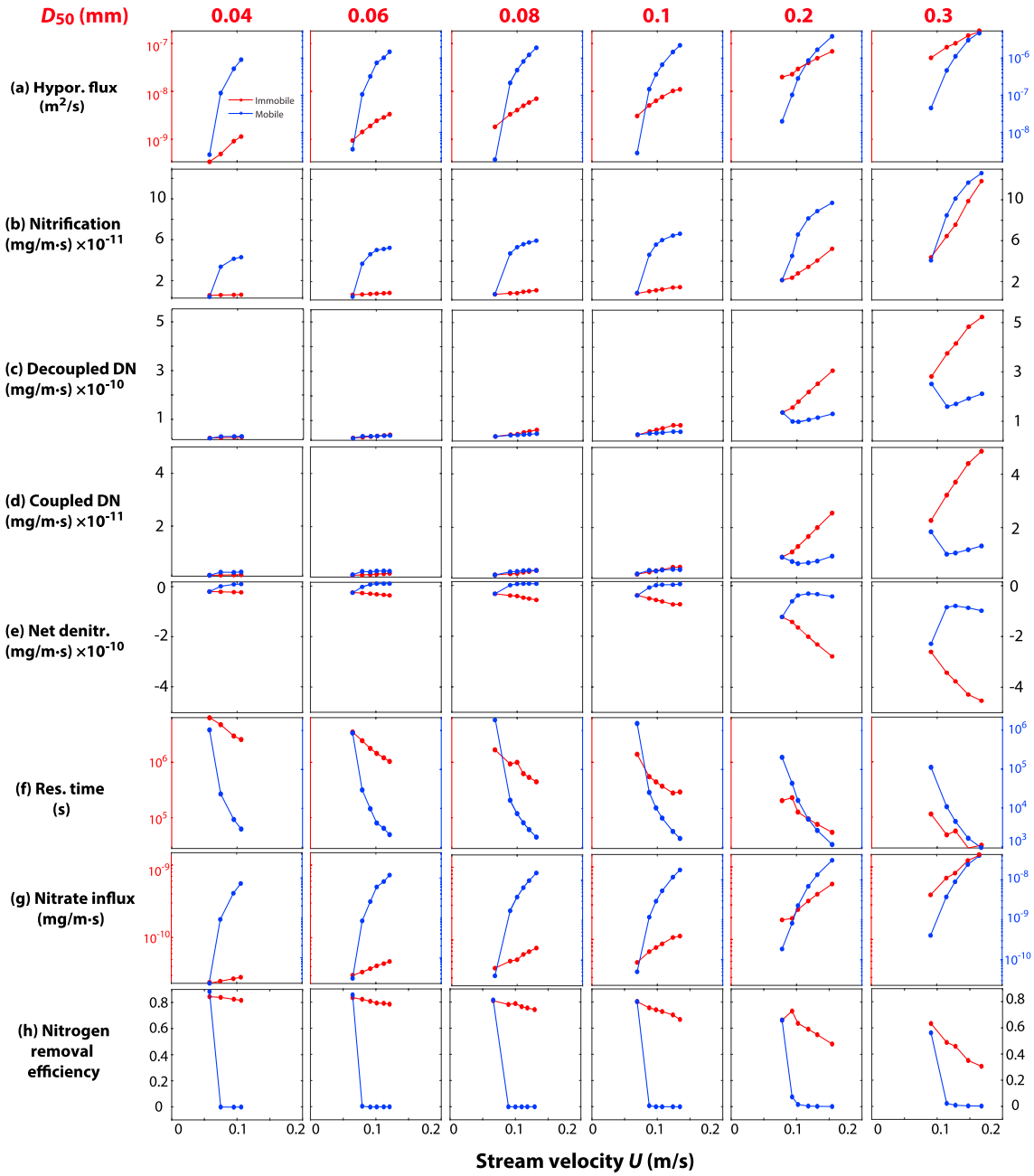

Figure 4. Comparison of various metrics for hyporheic zone processes between immobile and mobile bed form simulations: (a) integrated nitrification rate, (b) integrated denitrification rate, (c) net denitrification ((b) subtracted from (a); negative being net nitrifying), (d) flux of nitrate from the river into the hyporheic zone, (e) nitrogen removal efficiency, (f) ratio of hyporheic exchange flux, and (g) ratio of hyporheic exchange residence time.

fronts with increasing U, unlike in the mobile bed forms where the deepening of the solute front is muted with increase in U (and concurrently c).

The simulation conditions all had ample DOC. DOC hence penetrated deeper relative to the other reacting solutes with increasing U. This result includes the mobile cases. The other solutes (DO, NO_3^-, and NH_4^+) showed very similar behavior—they are mostly consumed within the migrating ripple, except for minor amounts which disperse beyond the depth of the trough. Thus, the vertical extent of the HZ from both physical (defined by flow paths) and chemical (defined by solute distribution) perspectives changed profoundly between mobile and immobile ripples. Whereas, the HZ extent ordinarily scales with the bed form length,

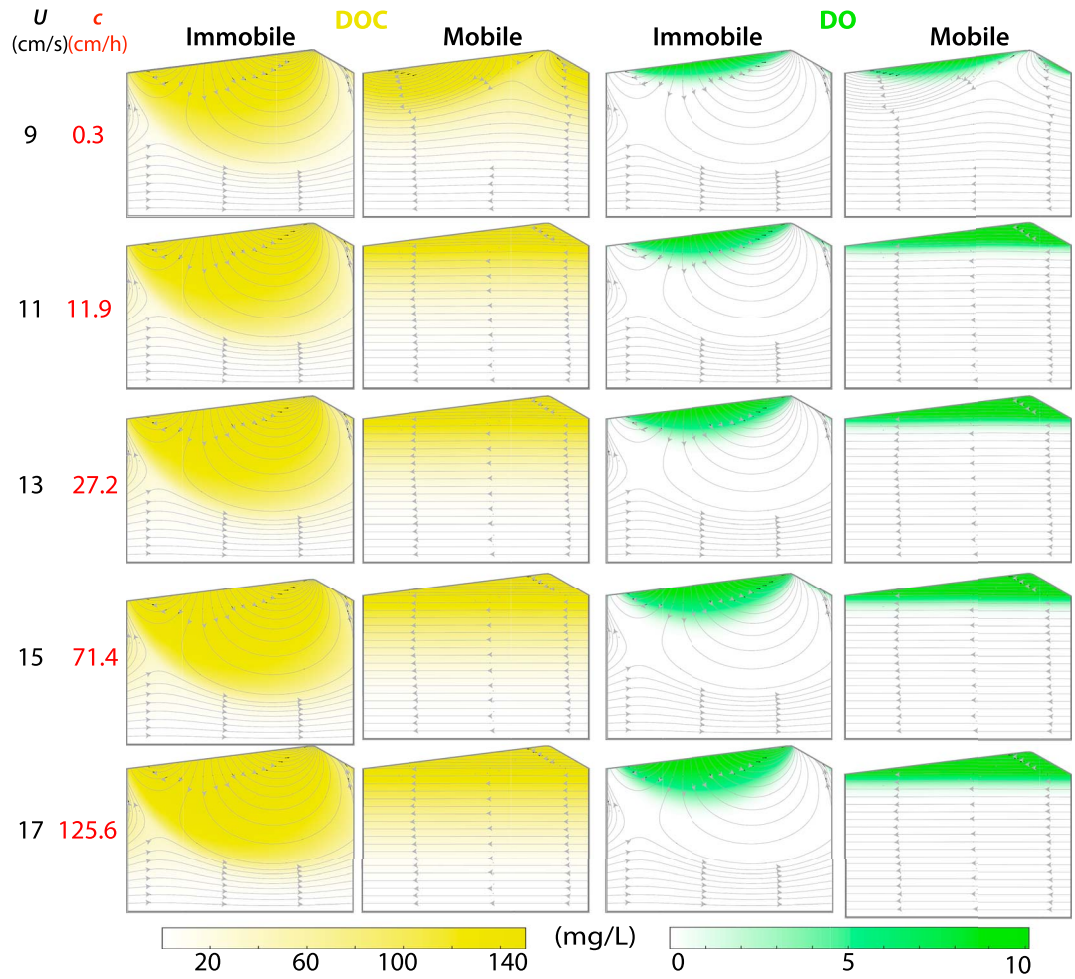

Figure 5. Simulated dissolved organic carbon (DOC) and dissolved oxygen (DO) fields for immobile and mobile bed forms across increasing mean channel velocity (U) and celerity (c) for the mobile cases. Gray lines are flow lines. The results are from the case "geometry 6" which has a $D_{50} = 0.3$ mm, $L = 157$ mm, and $\Delta = 16$ mm.

that is, hyporheic flow paths reach a depth that is similar to the wavelength of the bed form, for the mobile ripples, it is constrained by the ripple height when the ripple starts migrating. This difference would manifest for a conservative solute which would flush the entire HZ as well. For the reactive solutes considered, their penetration depths do not reach the full extent of the HZ, especially for the immobile, pure-pumping hyporheic exchange, ripples (Figures 5 and 6). At low U, the vertical extent of reactive solutes between the mobile and immobile cases can be quite similar. However, with increasing U, the solutes are pumped and advected deeper within the HZ of the immobile ripple, whereas the solutes cannot go any deeper when turnover is dominant in the fast-moving ripples.

The penetration depths of the solute plumes were also different. At low U and associated c, there was a trivial difference between mobile and immobile bed form HZs. With further increases in stream velocity and thus hyporheic exchange flux, the penetration depth of the solutes increased for the immobile bed form (Figures 5 and 6). However and unlike the immobile cases, the penetration depth of each solute decreased with increasing U and increasing c for the mobile bed form (Figures 5 and 6). In addition, the penetration depth was relatively smaller (10–20 cm) for the mobile bed form with the same U (Figures 5 and 6).

3.4. Impact of Bed Form Celerity on Denitrification and Nitrification

The mobile and immobile bed forms led to different effects on solute distribution, and thus also controlled the biogeochemical reaction zones differently. Here we focus on the individual species and their individual and integrated (or net) reaction rates.

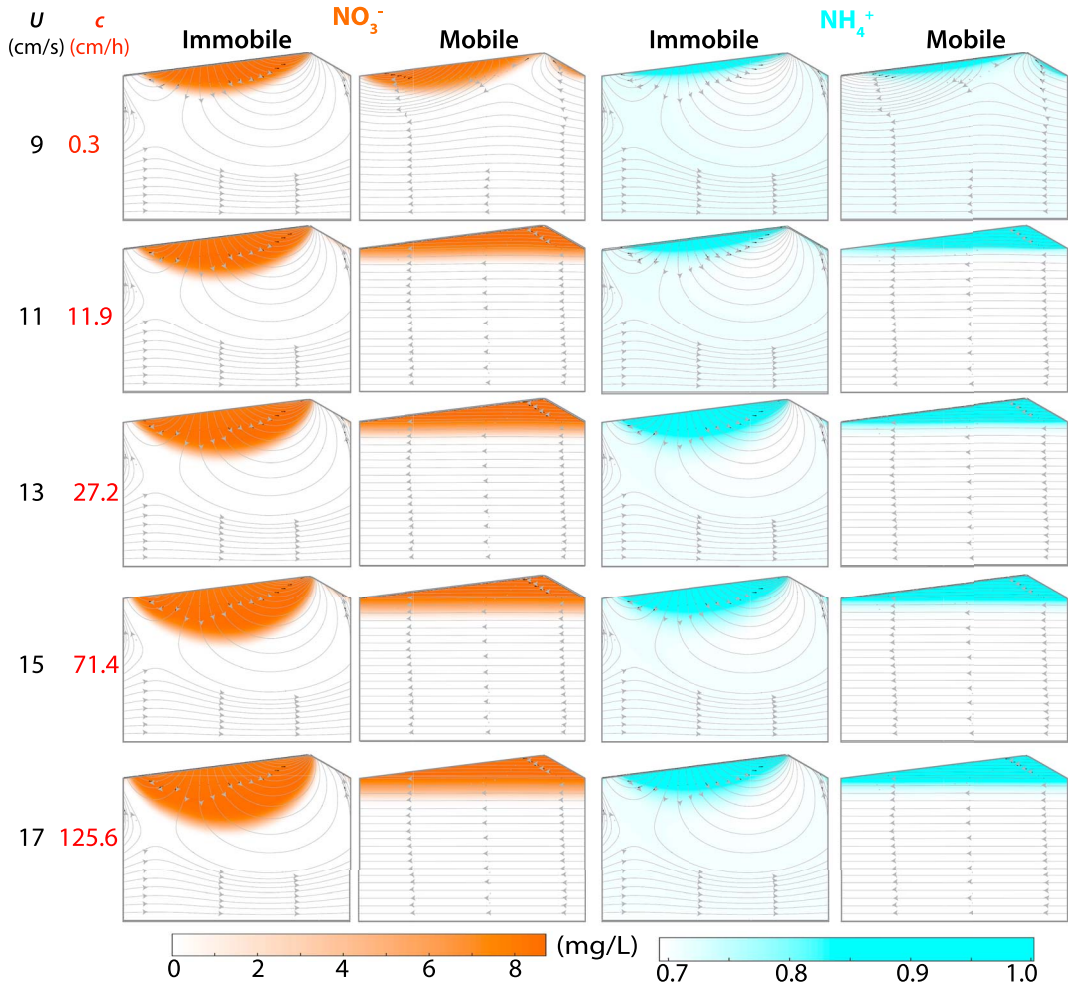

Figure 6. Simulated nitrate (NO_3^{2-}) and ammonium (NH_4^+) fields for immobile and mobile bed forms across increasing mean channel velocity (U) and celerity (c) for the mobile cases. Gray lines are flow lines. The results are from the case "geometry 6" which has a $D_{50} = 0.3$ mm, $L = 157$ mm, and $\Delta = 16$ mm.

For the immobile bed forms, the $NH_4^+$and DO distributions had a crescent-shape as noted previously (Figures 5 and 6). The nitrification zone expectedly followed the DO distribution (Figure 7). Moreover, the nitrification zone penetrated into deeper areas as U increased for the immobile bed form. Like the nitrification zone, the denitrification zone also became deeper with increasing U, and the deepest part shifted from the left of the domain at low U to the right at high U (Figure 7). The distribution of DO regulated both the nitrification and denitrification zones.

For the mobile bed form cases with three flow cells (the smallest celerity), the denitrification zones were two separate crescent-shaped zones. These two zones are split and meet at the crest of the bed form (Figure 7). For the rest of the mobile cases considered, where turnover dominated, nitrification zone changed from crescent-shaped zone to triangle-shaped zone with increasing U.

The denitrification zone was slightly shallower in the slowest-migrating mobile case when compared to the immobile case (Figure 7). There were trivial changes in the denitrification zone size for the immobile bed form with increasing U. The denitrification zone in the other mobile bed forms was a horizontal strip at the edge of the DO plume (see Figure 6). This strip moved gradually deeper and became thicker (more disperse) with increasing U.

Coupled denitrification was minor relative to decoupled (or direct) denitrification in all mobile and immobile bed forms cases considered (Figure 8); the latter is about 10 times as large as the former. This is because our simulations had relatively high concentrations of NO_3^- coming from the stream. The internally

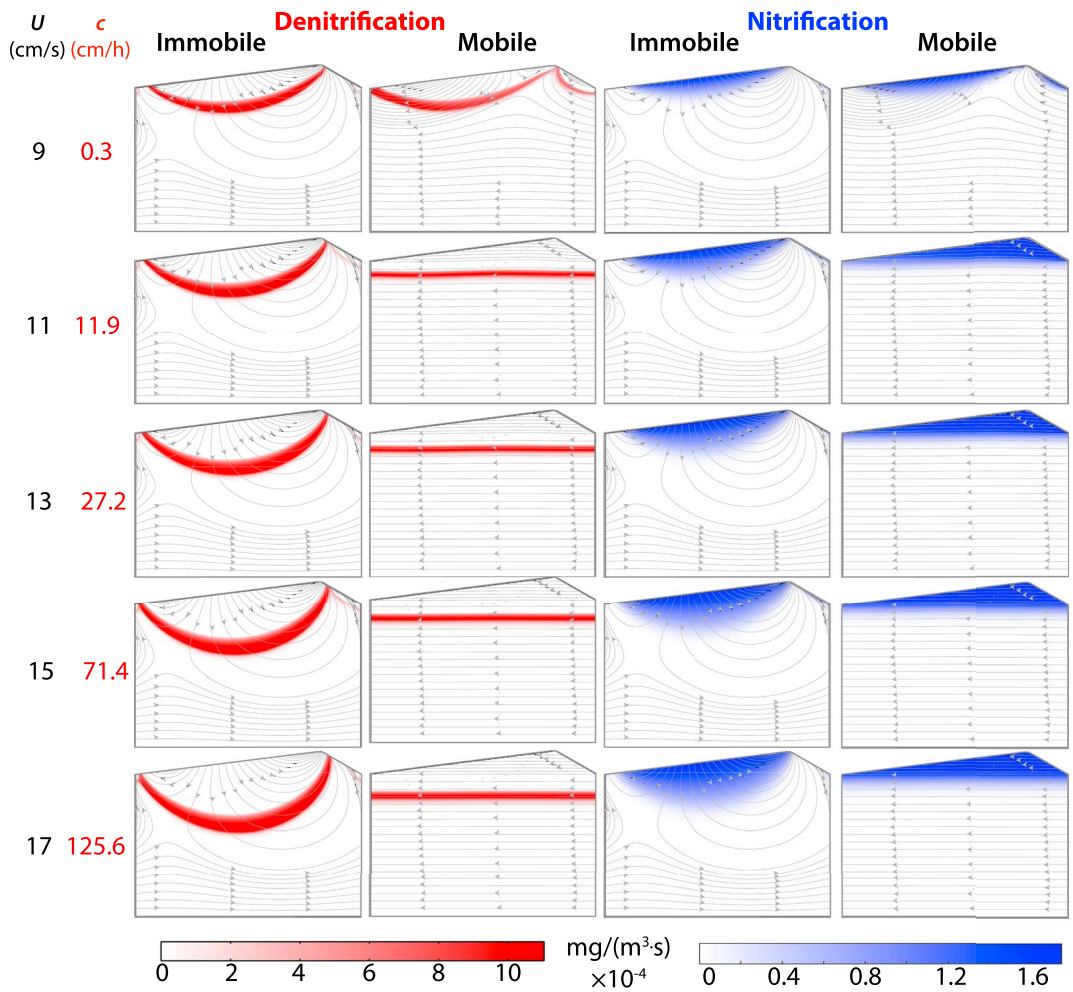

Figure 7. Distribution of simulated denitrification and nitrification rates for immobile and mobile bed forms across increasing mean channel velocity (U) and celerity (c) for the mobile cases. Gray lines are flow lines. The results are from the case "geometry 6" which has a D_{50} = 0.3 mm, L = 157 mm, and Δ = 16 mm.

produced NO_3^- was denitrified at slightly deeper depths (or further down the flowpaths) relative to the stream-sourced NO_3^-. However, the reaction zones are mostly overlapping since the reaction is very sensitive to where DO is ultimately diminished.

We integrated nitrification rates and denitrification rates over the entire domain to assess the over-all functionality of the HZ with respect to nitrogen cycling. This is the spatial integration of the fields shown in Figure 7. The results of this are presented in Figures 4b–4d. As expected, nitrification rates over the entire HZ (overall nitrification) increased monotonically with increasing U for both immobile and mobile cases (Figure 4b and Table S2). This was observed for all other ripple geometries (grain sizes) considered. This is expected since more oxygen and NH_4^+ are advected into the HZ with increasing U (and c).

For the immobile bed form, the overall denitrification increased monotonically with increasing U (Figures 4c and 4d and Table S2). For the mobile ripple cases, the overall denitrification generally increased with increasing U (and thus c; Figures 4c and 4d and Table S2). This overall increase is also evident as the expansion of the horizontal hot spot for denitrification (Figure 7). The overall coupled denitrification is generally about an order of magnitude smaller than coupled denitrification in all cases (immobile and mobile) considered (compare Figures 4c and 4d, and note the differences in axis scale).

The difference between the overall denitrification and nitrification shows that almost all the mobile cases simulated were net denitrifying or denitrification dominant (Figure 4e and Table S2). The mobile ripples with smaller D_{50} (those where $\leq$0.2 mm) were mostly net nitrifying at low to intermediate U. When D_{50} > 0.2 mm, the mobile ripples were also net denitrifying.

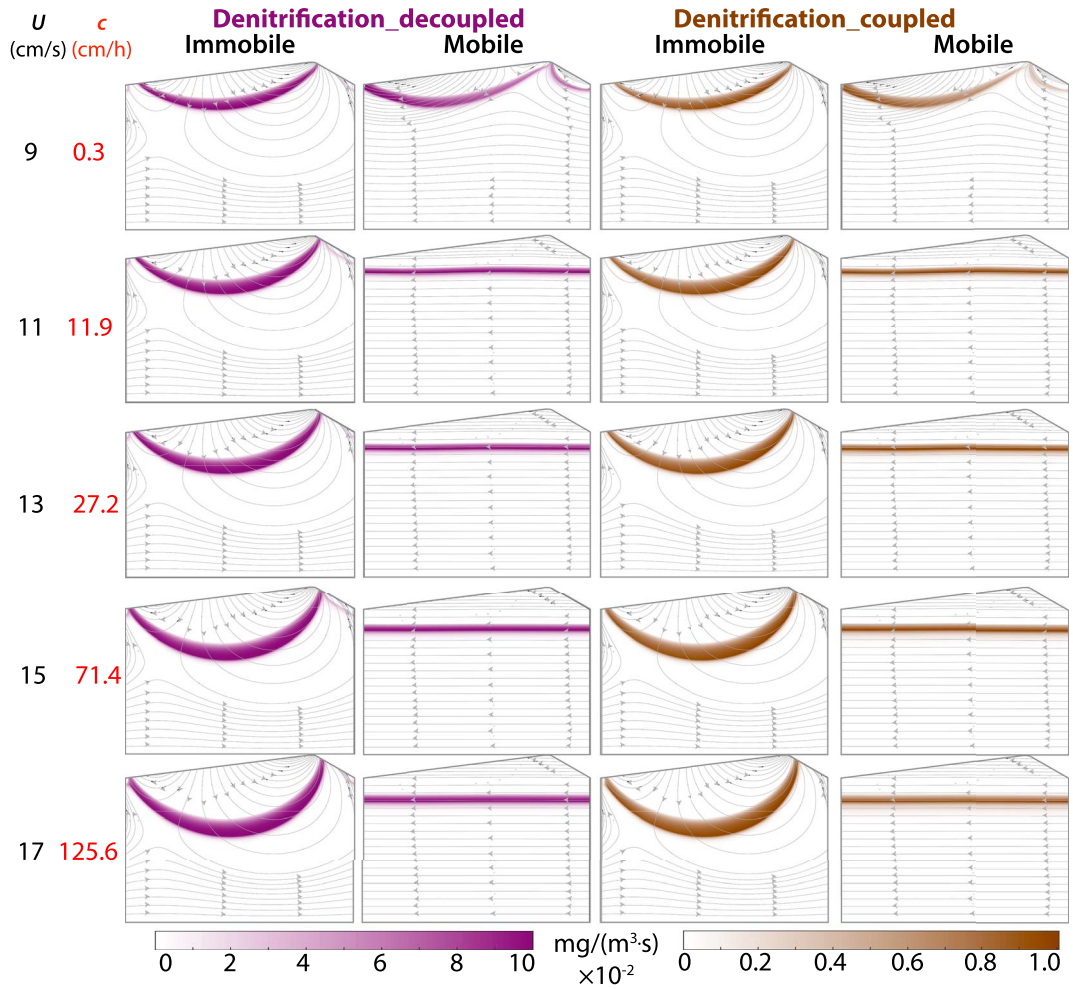

Figure 8. Distribution of decoupled and coupled denitrification for immobile and mobile bed forms across increasing mean channel velocity (U) and celerity (c) for the mobile cases. Gray lines are flow lines. The results are from the case "geometry 6" which has a $D_{50} = 0.3$ mm, $L = 157$ mm, and $\Delta = 16$ mm.

The nitrogen removal efficiency (N_{RE}) is a dimensionless number that describes the ability of the HZ to remove or retain nitrate. It is defined as the ratio of net denitrification rate (N_A) with the total influx of NO_3^- into the HZ (Zheng et al., 2016):

$$N_{RE} = \frac{|N_A|}{\left|\left[NO_3^-\right]_{in}\right|} \tag{34}$$

Because hyporheic exchange fluid flux, and thus also nitrate influx, continually increases with U, nitrogen removal efficiency was found to decrease with U. A smaller proportion of nitrate that went in the HZ was denitrified, and the HZ becomes oversupplied with nitrate which simply passes through the HZ (Figure 6). The mobile ripples had very low (~0) N_{RE} (Figure 4h). That is, while these moving ripples can denitrify more than they nitrify, the amount of nitrate consumed is relatively small compared to the nitrate influx. This is because turnover fluxes can be quite high.

4. Further Analysis and Discussion

4.1. Controls on Residence Time by Stream Velocity and Mean Grain Size

Biogeochemical and ecological transformations in HZs depend on the time scale of hyporheic exchange (Briggs et al., 2013, 2014; Cardenas et al., 2008; Gu et al., 2007; Marzadri et al., 2013; Zarnetske et al.,

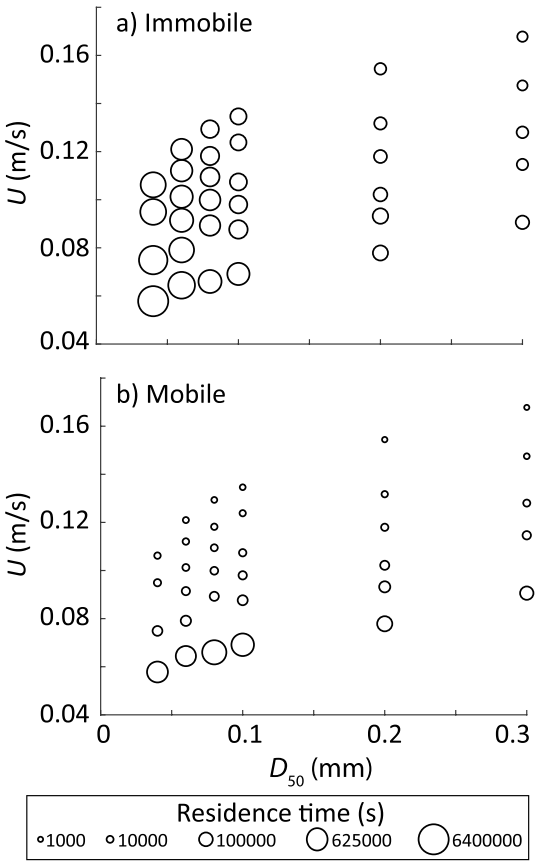

Figure 9. Hyporheic flow residence times for (a) immobile and (b) mobile ripples with different grain size (D_{50}) and stream velocity (U). The colors correspond with the same cases and color scheme in Figures 1 and 9.

2011). Residence time is therefore a useful metric and predictor for the potential biogeochemical function of the HZ as it controls the extent of biogeochemical transformation efficiency within the HZ (Haggerty et al., 2002). To further assess nitrate dynamics in the HZ, we quantitatively analyzed the residence time. There are numerous factors affecting the residence time of HZs, such as bed form asymmetry (Cardenas et al., 2008); hydraulic conductivity, valley slope, and sinuosity (Gomez et al., 2012); heterogeneity (Sawyer & Cardenas, 2009); and alluvial geomorphic features (Briggs et al., 2014). We focused on the effect of stream velocity and D_{50} since they essentially control the other factors, including hydraulic conductivity and bed form shape. We estimated and compared bulk residence times, $\bar{\tau}_{out}$, for the immobile and mobile bed forms with varying geometries or mean stream velocity following section 2.3.

D_{50} has a dominant role compared to U in controlling $\bar{\tau}_{out}$ for both mobile and immobile ripples (Figure 9). This is expected from Darcy's law. That is, pore velocity in the sediment is determined by the hydraulic conductivity and fluid pressure gradient via a linear relationship. Stream velocity in turn dictates the interface pressure gradient along the SWI. For immobile bed forms, hyporheic flux depends on stream Reynolds Number via a quadratic relationship (Elliott & Brooks, 1997a, 1997b; Cardenas & Wilson, 2007). Moreover, our approach assumed that permeability is related with D_{50} via a quadratic equation (Gangi, 1985). The U and D_{50}, which also dictates ripple geometry, thus play similar and complementary roles in regulating the pore velocity and subsequently $\bar{\tau}_{out}$ (Figure 9).

4.2. The Damköhler Number and Nitrogen Cycling

Following equation (33), $\bar{\tau}_{out}$ was used further to calculate the Damköhler number (Da) while assuming a constant k_{DOC}. When $Da < 1$, chemical reactions dependent on DOC would be rate-limited due to the brevity of the time that DOC spends within the HZ. At this low Da, the HZ stays oxic and thus nitrification should be high with little to no denitrification; the HZ is net nitrifying. When $Da > 1$, the residence time is greater than the reaction time. Under these conditions, DOC can be exhausted, forming a pronounced anoxic zone below and past the zone of high respiration. However, the DOC exhaustion would lead to the cessation of further denitrification, a process favored in the anoxic zone. This supply-limited situation would lead to a constantly low denitrification rate when $Da > 1$. Thus, generally, nitrification is dominant at low Da and denitrification dominates at high Da (Zarnetske et al., 2011, 2012). Implicit in the interpretation discussed above is that the chemical reaction time ($1/k_{\mathrm{DOC}}$) controls the denitrification rate if there is a constant and sufficient supply of reactants.

Not surprisingly, there is a strongly coherent relationship between the Da and hyporheic exchange flux (q_{HZ}; Figure 10a). Thus, we fitted a power function to the flux-Da results which led to

$$Da = a \cdot q_{\mathrm{HZ}}{}^{b} \tag{35}$$

where $a = 4.609 \times 10^{-7}$ (with 95% confidence bounds of 3.047×10^{-7} and 6.172×10^{-7}) and $b = -0.8348$ (with 95% confidence bounds of -0.8511 and -0.8185); the R^2 for the fit was 0.99. Reactant influx follows a similar relationship with Da since transport into the hyporheic zone is largely advective (Figure 10b).

Both mobile and immobile ripples exhibited a general reduction in bulk reaction rates with increasing Da (Figures 10c–10e). However, while most cases were net denitrifying regardless of Da, what is more relevant and revealing is the N_{RE} since this answers the question of whether the HZ helps buffer or remove nitrogen present in the river. The N_{RE} is generally <0.10 and usually vanishingly small when $Da < 0.05$. The lower Da situations correspond with the mobile ripples; the Da for these cases ranged from ~0 to 10.7 with a mean of

0.9, whereas the immobile ripples' Da ranged from ~0 to 32.1 with a mean of 5.7. The corresponding average N_{RE} are 0.03 and 0.44, for the mobile and immobile ripples, respectively.

The N_{RE} can be predicted from the Da through the fitted equation:

$$N_{RE} = a\left(1-\frac{1-e^{-b\cdot Da}}{b\cdot Da}\right) \tag{36}$$

where $a = 0.8302$ (with 95% confidence bounds of 0.803 and 0.8573) and $b = 4.185$ (with 95% confidence bounds of 3.7 and 4.67); the R^2 for the fit was 0.969. This equation, as well as the model result ranges, further highlights that mobile ripples are less efficient in removing nitrogen than their immobile counterparts.

Equations (35) and (36) provide the foundation for a predictive framework. If some model can be used to predict hyporheic exchange flux (e.g., Gomez-Velez & Harvey, 2014), the Da can also be estimated. From this Da, the N_{RE} can be predicted regardless of whether the ripples are migrating or not.

It is important to note that the biogeochemical setting we considered is net denitrifying. Some riverbeds may be net nitrifying and/or may be dominated by coupled nitrification-denitrification rather than direct denitrification (Azizian et al., 2017). However, our analysis reveals that even when turnover exchange is significant, coupled nitrification-denitrification is still small for net denitrifying situations. The results nonetheless show that even in the most favorable condition, the N_{RE} tops out at 0.83 (i.e., the scaling coefficient a in equation (36)). This limit arises from the competition between oxic and anoxic reactions. The capacity to bring nitrate into the HZ is always coupled with introduction of oxygen as well, which hinders denitrification and promotes nitrification.

4.3. Relationship With Previous Studies on Biogeochemical Reactions in HZs of Migrating Bed Forms

To our knowledge, there have been two other studies that investigated the effects of bed form migration on reactions within hyporheic zones. These are the investigations of Kessler et al. (2015) and Ahmerkamp et al. (2015). Ahmerkamp et al. (2015) demonstrated that bed form migration strongly attenuated benthic oxygen fluxes and penetration depth. However, that study did not analyze the potential effect on denitrification or any nitrogen reactions, which is the focus of our study. Hence, comparisons are difficult. But since denitrification of the HZ is closely related to oxygen fluxes in the HZ, this suggests that bed form migration should have an effect on denitrification of the HZ.

The investigation by Kessler et al. (2015) who studied the potential effect of the bed form celerity on denitrification by comparing stationary and migrating ripples with different mean flow velocities is more directly comparable to our research. That study concluded that bed form migration has a negligible effect on denitrification of the HZ. Unfortunately, there are many differences between Kessler et al. (2015) and our current study that prevents a meaningful direct comparison. The model by Kessler et al. (2015) was designed for coastal or beach sediment. In these environments, there is typically low DOC in the seawater, and the water is generally oligotrophic. On the other hand, our aquatic situation was more nutrient rich and the nitrate concentration for the overlying water we assumed was about 5 times that in Kessler et al. (2015). The outcomes of reactive transport modeling of nitrogen cycling is very sensitive to the ratio $[NO_3^-]/[NH_4^+]$ (Zheng et al., 2016). In this study, the ratio is 8, while it was 40 in Kessler et al. (2015), so these studies represent very different settings. Our numerical modeling experiments were designed to isolate the reactions of incoming hyporheic water borne-solutes, whereas Kessler et al. (2015) was constrained by a variety of experimental and field observations that relate to the rippled coastal sediment they were hoping to represent. One crucial process they considered was mineralization which linearly controlled respiration, denitrification, and ammonification. However, to our knowledge, similar to our approach, mineralization is not typically considered in the reactive transport modeling of aquatic hyporheic zones (e.g., Gu et al., 2007; Marzadri et al., 2011; Trauth et al., 2014; Zarnetske et al., 2012), although some of these models consider the leaching of DOC from particulate organic carbon as a distributed source term. The way mineralization is represented in Kessler et al. (2015) has the effect that there is substrate available everywhere for the reactions; in particular, this renders the system as not carbon limited. In our case, the incoming DOC is necessary to trigger the cascade of redox reactions. Incidentally, Kessler et al. (2015) also included ammonification in their model, whereas just like other hyporheic zone reactive transport modeling studies (Gu et al., 2007; Marzadri

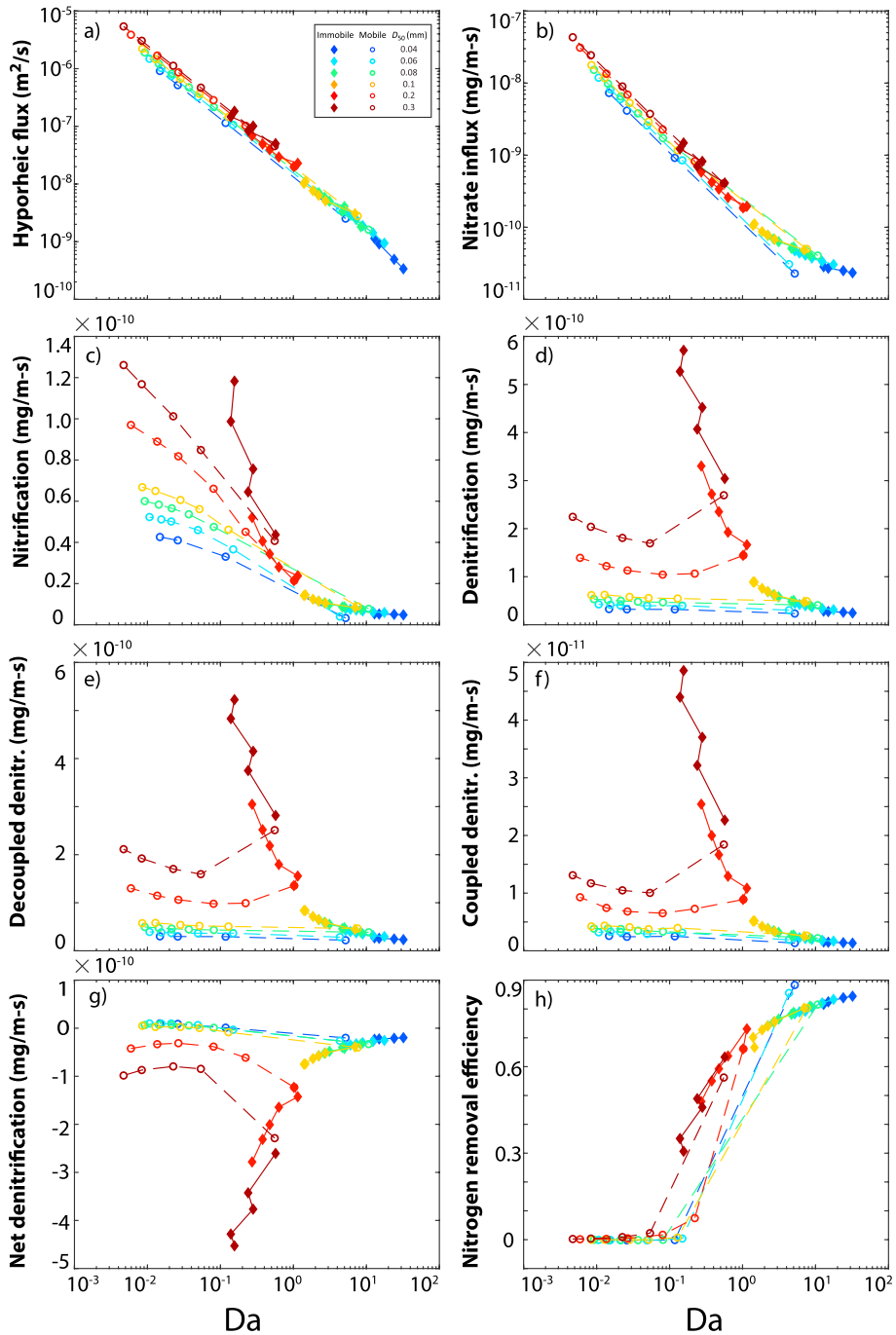

Figure 10. Simulated fluid and solute fluxes and reaction rates across varying Damköhler number (*Da*) conditions. The different symbols and colors correspond to bed form mobility and grain size. The colors correspond with the same cases and color scheme in Figures 1 and 8.

et al., 2011; Trauth et al., 2014; Zarnetske et al., 2012) we did not. The ammonification thought to be important for the coastal sediment that Kessler et al. (2015) studied has also been considered in other aquatic hyporheic zone models (e.g., Azizian et al., 2015, 2017). There are thus many fundamental differences in how the biogeochemistry is handled between our study and Kessler et al. (2015) that make the studies hard to compare.

Kessler et al. (2015) assumed a flat bed surface and imposed a pressure on the horizontal sediment-water interface. This inhibits the potential flux from the leeside of the bed form due to turnover. This would add further differences between our study and theirs. It is not surprising therefore that while Kessler et al. (2015) concluded that bed form migration has a negligible effect on overall denitrification, our simulations showed a different outcome. Ripple migration may matter a lot for HZ biogeochemistry for some ripples that are constructed following a morphodynamically consistent framework. Neither this study nor Kessler et al. (2015) is the last word on this topic since both studies have only treated a small subset of many possible scenarios.

4.4. Implications and Limitations of the Study

A riverbed very rarely has only a single repeating ripple bed form, if that is even possible, as we assumed. But it is typical that small bed forms are superimposed over large bed forms, that is, ripples on top of dunes (Jerolmack & Mohrig, 2005; Venditti et al., 2005). Yet despite constant evolution of sandy riverbeds, their topography exhibits a statistical steady state; dynamic bed form topography is scale invariant and statistically stationary (Jerolmack & Mohrig, 2005). Moreover, sediment transport of larger-scale bed forms, that is, dunes, can be considered simply as the sum of the transport of the small-scale bed forms, that is, ripples (Venditti et al., 2005). The larger dunes migrate by the translation of the ripples on their backs (Jerolmack & Mohrig, 2005). Thus, migrating ripples are perhaps the most fundamental and relevant roughness element of dynamic sandy riverbeds.

Ripples, or in general, shorter-wavelength topographic roughness elements are also responsible for forcing the most hyporheic exchange flux especially given fractal bed topography (Wörman et al., 2007). What happens in a statistically representative ripple can thus be sufficient for explaining an entire field. Such an approach would capture the critical aspects of the interrelated morphodynamic, hydraulic, and biogeochemical processes.

The biogeochemical reactions and perhaps some of the transport aspects we modeled are still poorly constrained, partly owing to lack of empirical studies. We ignored sorption of ammonium for example. This would obviously directly impact nitrification, and thus also denitrification, but only for transient conditions. For the steady state conditions which our model solved, sorption is irrelevant. Furthermore, our framework ignored ammonification. Sorption of ammonium and its production through ammonification would lead to a situation where there is ammonium pool intrinsic to the sediment, and this would be present even when the sediment migrating; that is, it would still be relevant for migrating ripples.

The design of the models in this study is such that the reactions of river-borne solutes entering the HZ are analyzed in isolation. This is idealized and hypothetical. Many real situations would have resident water in the HZ that may have a different chemistry as the water being exchanged and entering the sediment. There might also be ambient groundwater flow into or out from the river (Hester et al., 2017, 2019); that is, the river could either be under gaining or losing conditions (it is neutral in the models here). Any mixing of hyporheic water with ambient groundwater could entirely change the cascade of reactions.

The models ignored heterogeneity of the sediment hydraulic and transport properties at the scale of several centimeters (larger than dispersivity). However, a few studies have shown that mild heterogeneity (and this magnitude might be expected for a single ripple) does not have a substantial impact on overall hyporheic zone reactive transport (Bardini et al., 2013). Aside from this macroscale heterogeneity, there is also microscale heterogeneity. There might be anoxic microsites in an otherwise oxic environment within the sediment. These microsites could host reducing redox processes such as denitrification. Studies have suggested that these microsites integrate to impact bed form-scale reactions (Briggs et al., 2015, 2018; Harvey et al., 2013; Kessler et al., 2014; Sawyer, 2015). The connected processes noted above are complicating factors not considered in this study.

While our approach provides a way for estimating bulk residence time (or Damköhler number) for a migrating ripple, there remains much uncertainty with reaction time scales, that is, k_{DOC}. A riverbed with fractal topography also exhibits multiscale hyporheic flow paths (Wörman et al., 2007) which produce power law residence time distributions. An individual ripple or bed form already has a power law residence time distribution (Cardenas et al., 2008) and fractal riverbed topography or multiscale features serve to expand this distribution (Cardenas et al., 2008). The relative contributions of short- versus long-flow paths, or more

precisely between ripples and the dunes that they are superimposed on, to overall reaction rates remain to be investigated. If the reactions of interest are determined by shorter residence times (or occur within shallower flow paths) such as the aerobic reactions of respiration and nitrification, then our model focused on ripples might suffice in predicting them. Intermediate- to long-time reactions occurring in the suboxic to anoxic zone, that is, denitrification, may be particularly sensitive to any elongation (or contraction) of the residence time distribution. Our results indicate that bed form migration reduces residence times and thus a migrating bed form field with a range in scale of roughness features might also have overall shorter residence times relative to the same bed configuration but with an immobile bed. Will the migration of an entire bed form field also lead to smaller separate hyporheic flow cells each with relatively shorter residence times? How sensitive are the bulk reaction rates to these subtle changes, and in turn can subtle changes in reaction parameters (e.g., k_{DOC}) affect this sensitivity? Migrating ripples may also host different microbial communities relative to fixed ones. Such differences can profoundly affect biologically mediated chemical reactions. These open problems can potentially be tackled in future research that applies the concepts and approaches introduced here to migrating multiscale bed form fields.

5. Summary and Conclusions

We studied the effect of bed form morphodynamics on nitrogen processing in the hyporheic zone of ripples by comparing paired flow and reactive simulations of fixed and migrating ripples. We built realistic ripple geometry following bed form stability regimes and other criteria for ripple formation. Bed form celerity or migration rate was determined by streamflow velocity. Six ripple geometries with different sediment grain sizes and flow velocities and migration rates were studied through multiphysics numerical simulations of turbulent river flow, hyporheic flow of porewater through the sediment, and reactive transport of carbon, oxygen, and nitrogen. The results showed that the turnover effect due to bed form migration dramatically changed the hyporheic flow field, hyporheic exchange flux, solute distribution, and biogeochemical reactions in the hyporheic zone. The dependence of overall solute reaction rates on bed form migration, grain size, and ripple geometry was nontrivial (nonlinear and sometimes nonmonotonic). We found however that in general the nitrate removal efficiency increased with the Damköhler number following an asymptotic behavior for both mobile and immobile bed forms. Assuming immobile bed forms overestimates nitrate removal efficiency, especially for cases with fine sediments when migration-driven turnover hyporheic exchange is dominant over current-topography interaction-driven pumping exchange. The relationship between nitrate removal efficiency and Damköhler number established here can be used to predict nitrogen processing at the river corridor scale.

Acknowledgments
This research is supported by the U.S. Department of Energy (DOE), Office of Biological and Environmental Research (BER), as part of BER's Subsurface Biogeochemical Research Program (SBR) under award DE-SC0018042. The experimental conditions and associated results are all presented in Tables S1 and S2; data from these tables, including the calculations of some metrics, are also provided in a Microsoft Excel spreadsheet. We thank Erich Hester, Stanley Grant, and Judson Harvey for the thoughtful and constructive comments on earlier versions of this manuscript.

References

Ahmerkamp, S., Winter, C., Janssen, F., Kuypers, M. M., & Holtappels, M. (2015). The impact of bedform migration on benthic oxygen fluxes. *Journal of Geophysical Research: Biogeosciences*, *120*, 2229–2242. https://doi.org/10.1002/2015JG003106

Alexander, R. B., Smith, R. A., & Schwarz, G. E. (2000). Effect of stream channel size on the delivery of nitrogen to the Gulf of Mexico. *Nature*, *403*(6771), 758–761. https://doi.org/10.1038/35001562

Ashley, G. M. (1990). Classification of large-scale subaqueous bedforms: A new look at an old problem-SEPM bedforms and bedding structures. *Journal of Sedimentary Research*, *60*(1), 160–172. https://doi.org/10.1306/212F9138-2B24-11D7-8648000102C1865D

Azizian, M., Boano, F., Cook, P. L. M., Detwiler, R. L., Rippy, M. A., & Grant, S. B. (2017). Ambient groundwater flow diminishes nitrate processing in the hyporheic zone of streams. *Water Resources Research*, *53*, 3941–3967. https://doi.org/10.1002/2016WR020048

Azizian, M., Grant, S. B., Kessler, A. J., Cook, P. L. M., Rippy, M. A., & Stewardson, M. J. (2015). Bedforms as biocatalytic filters: A pumping and streamline segregation model for nitrate removal in permeable sediments. *Environmental Science & Technology*, *49*(18), 10,993–11,002. https://doi.org/10.1021/acs.est.5b01941

Bardini, L., Boano, F., Cardenas, M. B., Revelli, R., & Ridolfi, L. (2012). Nutrient cycling in bedform induced hyporheic zones. *Geochimica et Cosmochimica Acta*, *84*, 47–61. https://doi.org/10.1016/j.gca.2012.01.025

Bardini, L., Boano, F., Cardenas, M. B., Sawyer, A. H., Revelli, R., & Ridolfi, L. (2013). Small-scale heterogeneity has negligible effects on nutrient cycling in streambeds. *Geophysical Research Letters*, *40*, 1118–1122. https://doi.org/10.1002/grl.50224

Birgand, F., Skaggs, R. W., Chescheir, G. M., & Gilliam, J. W. (2007). Nitrogen removal in streams of agricultural catchments—A literature review. *Critical Reviews in Environment Science and Technology*, *37*(5), 381–487. https://doi.org/10.1080/10643380600966426

Boano, F., Demaria, A., Revelli, R., & Ridolfi, L. (2010). Biogeochemical zonation due to intrameander hyporheic flow. *Water Resources Research*, *46*, W07535. https://doi.org/10.1029/2008WR007583

Boano, J., Harvey, W., Marion, A., Packman, A. I., Revelli, R., Ridolfi, L., & Wörman, A. (2014). Hyporheic flow and transport processes: Mechanisms, models, and biogeochemical implications. *Reviews of Geophysics*, *52*, 603–679. https://doi.org/10.1002/2012RG000417

Bottacin-Busolin, A., & Marion, A. (2010). Combined role of advective pumping and mechanical dispersion on time scales of bed form-induced hyporheic exchange. *Water Resources Research*, *46*, W08518. https://doi.org/10.1029/2009WR008892

Boulton, A. J., Findlay, S., Marmonier, P., Stanley, E. H., & Valett, H. M. (1998). The functional significance of the hyporheic zone in streams and rivers. *Annual Review of Ecology and Systematics*, *29*(1), 59–81. https://doi.org/10.1146/annurev.ecolsys.29.1.59

Briggs, M. A., Day-Lewis, F. D., Dehkordy, F. M. P., Hampton, T., Zarnetske, J. P., Scruggs, C. R., et al. (2018). Direct observations of hydrologic exchange occurring with less-mobile porosity and the development of anoxic microzones in sandy lakebed sediments. *Water Resources Research*, *54*(7), 4714–4729. https://doi.org/10.1029/2018WR022823

Briggs, M. A., Day-Lewis, F. D., Zarnetske, J. P., & Harvey, J. W. (2015). A physical explanation for the development of redox microzones in hyporheic flow. *Geophysical Research Letters*, *42*, 4402–4410. https://doi.org/10.1002/2015GL064200

Briggs, M. A., Lautz, L. K., & Hare, D. K. (2014). Residence time control on hot moments of net nitrate production and uptake in the hyporheic zone. *Hydrological Processes*, *28*(11), 3741–3751. https://doi.org/10.1002/hyp.9921

Briggs, M. A., Lautz, L. K., Hare, D. K., & González-Pinzón, R. (2013). Relating hyporheic fluxes, residence times, and redox-sensitive biogeochemical processes upstream of beaver dams. *Freshwater Science*, *32*(2), 622–641. https://doi.org/10.1899/12-110.1

Buffington, J. M., & Tonina, D. (2009). Hyporheic exchange in mountain rivers: II—Effects of channel morphology on mechanics, scales, and rates of exchange. *Geography Compass*, *3*(3), 1038–1062. https://doi.org/10.1111/j.1749-8198.2009.00225.x

Butturini, A., Battin, T. J., & Sabater, F. (2000). Nitrification in stream sediment biofilms: The role of ammonium concentration and DOC quality. *Water Research*, *34*(2), 629–639. https://doi.org/10.1016/S0043-1354(99)00171-2

Cardenas, J., Wilson, L., & Haggerty, R. (2008). Residence time of bedform-driven hyporheic exchange. *Advances in Water Resources*, *31*(10), 1382–1386. https://doi.org/10.1016/j.advwatres.2008.07.006

Cardenas, M. B. (2008). Surface water-groundwater interface geomorphology leads to scaling of residence times. *Geophysical Research Letters*, *35*, L08402. https://doi.org/10.1029/2008GL033753

Cardenas, M. B. (2015). Hyporheic zone hydrologic science: A historical account of its emergence and a prospectus. *Water Resources Research*, *51*, 3601–3616. https://doi.org/10.1002/2015WR017028

Cardenas, M. B., & Wilson, J. L. (2007). Dunes, turbulent eddies, and interfacial exchange with permeable sediments. *Water Resources Research*, *43*, W08412. https://doi.org/10.1029/2006WR005787

Coleman, S. E., & Melville, B. W. (1994). Bed-form development. *Journal of Hydraulic Engineering*, *120*(5), 544–560. https://doi.org/10.1061/(ASCE)0733-9429(1994)120:5(544)

Craig, L. S., Palmer, M. A., Richardson, D. C., Filoso, S., Bernhardt, E. S., Bledsoe, B. P., et al. (2008). Stream restoration strategies for reducing river nitrogen loads. *Frontiers in Ecology and the Environment*, *6*(10), 529–538. https://doi.org/10.1890/070080

Elliott, A. H., & Brooks, N. H. (1997a). Transfer of nonsorbing solutes to a streambed with bed forms: Theory. *Water Resources Research*, *33*(1), 123–136. https://doi.org/10.1029/96wr02784

Elliott, A. H., & Brooks, N. H. (1997b). Transfer of nonsorbing solutes to a streambed with bed forms: Laboratory experiments. *Water Resources Research*, *33*(1), 137–151. https://doi.org/10.1029/96wr02783

Fischer, H., Kloep, F., Wilzcek, S., & Pusch, M. (2005). A river's liver—Microbial processes within the hyporheic zone of a large lowland river. *Biogeochemistry*, *76*(2), 349–371. https://doi.org/10.1007/s10533-005-6896-y

Galloway, J. N. (1998). The global nitrogen cycle: Changes and consequences. *Environmental Pollution*, *102*(1), 15–24. https://doi.org/10.1016/S0269-7491(98)80010-9

Gangi, A. F. (1985). Permeability of unconsolidated sands and porous rocks. *Journal of Geophysical Research*, *90*(B4), 3099–3104. https://doi.org/10.1029/JB090iB04p03099

García, M. H. (2008). Sediment transport and morphodynamics, Sedimentation engineering: Processes, measurements, modeling, and practice. In *ASCE Manual*, (Vol. 110, chap. 2, p. 94). New York: American Society of Civil Engineers, ISBN 10 # 0784408149. https://doi.org/10.1061/40856(200)94

Gomez, J. D., Harvey, J. W., Cardenas, M. B., & Kiel, B. (2015). Denitrification in the Mississippi River network controlled by flow through river bedforms. *Nature Geoscience*, *8*(12), 941–945. https://doi.org/10.1038/ngeo2567

Gomez, J. D., Wilson, J. L., & Cardenas, M. B. (2012). Residence time distributions in sinuosity-driven hyporheic zones and their biogeochemical effects. *Water Resources Research*, *48*, W09533. https://doi.org/10.1029/2012wr012180

Gomez-Velez, J. D., & Harvey, J. W. (2014). A hydrogeomorphic river network model predicts where and why hyporheic exchange is important in large basins. *Geophysical Research Letters*, *41*, 6403–6412. https://doi.org/10.1002/2014gl061099

Goode, D. J. (1996). Direct simulation of groundwater age. *Water Resources Research*, *32*(2), 289–296. https://doi.org/10.1029/95wr03401

Gruber, N., & Galloway, J. N. (2008). An Earth-system perspective of the global nitrogen cycle. *Nature*, *451*(7176), 293–296. https://doi.org/10.1038/nature06592

Gu, C., Hornberger, G. M., Mills, A. L., Herman, J. S., & Flewelling, S. A. (2007). Nitrate reduction in streambed sediments: Effects of flow and biogeochemical kinetics. *Water Resources Research*, *43*, W12413. https://doi.org/10.1029/2007WR006027

Haggerty, R., Wondzell, S. M., & Johnson, M. A. (2002). Power-law residence time distribution in the hyporheic zone of a 2nd-order mountain stream. *Geophysical Research Letters*, *29*(13), 1640. https://doi.org/10.1029/2002GL014743

Harvey, J., Böhlke, K., Voytek, M. A., Scott, D., & Tobias, C. R. (2013). Hyporheic zone denitrification: Controls on effective reaction depth and contribution to whole-stream mass balance. *Water Resources Research*, *49*, 6298–6316. https://doi.org/10.1002/wrcr.20492

Harvey, J., Drummond, R., Martin, L., McPhillips, A., Packman, D., Jerolmack, S., et al. (2012). Hydrogeomorphology of the hyporheic zone: Stream solute and fine particle interactions with a dynamic streambed. *Journal of Geophysical Research*, *117*, G00N11. https://doi.org/10.1029/2012JG002043

Harvey, J., & Gooseff, M. (2015). River corridor science: Hydrologic exchange and ecological consequences from bedforms to basins. *Water Resources Research*, *51*, 6893–6922. https://doi.org/10.1002/2015WR017617

Hester, E. T., Cardenas, M. B., Haggerty, R., & Apte, S. V. (2017). The importance and challenge of hyporheic mixing. *Water Resources Research*, *53*, 3565–3575. https://doi.org/10.1002/2016WR020005

Hester, E. T., Eastes, L. A., & Widdowson, M. A. (2019). Effect of surface water stage fluctuation on mixing-dependent hyporheic denitrification in riverbed dunes. *Water Resources Research*, *55*, 4668–4687. https://doi.org/10.1029/2018WR024198

Hunter, K. S., Wang, Y., & Van Cappellen, P. (1998). Kinetic modeling of microbially-driven redox chemistry of subsurface environments: Coupling transport, microbial metabolism and geochemistry. *Journal of Hydrology*, *209*(1-4), 53–80. https://doi.org/10.1016/S0022-1694(98)00157-7

Janssen, F., Cardenas, M. B., Sawyer, A. H., Dammrich, T., Krietsch, J., & Beer, D. (2012). A comparative experimental and multiphysics computational fluid dynamics study of coupled surface–subsurface flow in bed forms. *Water Resources Research*, *48*, W08514. https://doi.org/10.1029/2012WR011982

Jerolmack, D. J., & Mohrig, D. (2005). A unified model for subaqueous bed form dynamics. *Water Resources Research*, *41*, W12421. https://doi.org/10.1029/2005WR004329

Karim, F. (1995). Bed configuration and hydraulic resistance in alluvial-channel flows. *Journal of Hydraulic Engineering*, *121*(1), 15–25. https://doi.org/10.1061/(ASCE)0733-9429

Kaufman, M. H., Cardenas, M. B., Buttles, J., Kessler, A. J., & Cook, P. L. M. (2017). Hyporheic hot moments: Dissolved oxygen dynamics in the hyporheic zone in response to surface flow perturbations. *Water Resources Research*, *53*, 6642–6662. https://doi.org/10.1002/2016WR020296

Kessler, A. J., Cardenas, M. B., & Cook, P. L. M. (2015). The negligible effect of bed form migration on denitrification in hyporheic zones of permeable sediments. *Journal of Geophysical Research: Biogeosciences*, *120*, 538–548. https://doi.org/10.1002/2014JG002852

Kessler, A. J., Cardenas, M. B., Santos, I. R., & Cook, P. L. M. (2014). Enhancement of denitrification in permeable carbonate sediment due to intra-granular porosity: A multi-scale modelling study. *Geochimica et Cosmochimica Acta*, *141*, 440–453. https://doi.org/10.1016/j.gca.2014.06.028

Kiel, B. A., & Cardenas, M. (2014). Lateral hyporheic exchange throughout the Mississippi River network. *Nature Geoscience*, *7*(6), 413–417. https://doi.org/10.1038/ngeo2157

Lefebvre, A., Paarlberg, A. J., & Winter, C. (2014). Flow separation and shear stress over angle-of-repose bed forms: A numerical investigation. *Water Resources Research*, *50*, 986–1005. https://doi.org/10.1002/2013WR014587

Malzone, J. M., Lowry, C. S., & Ward, A. S. (2016). Response of the hyporheic zone to transient groundwater fluctuations on the annual and storm event time scales. *Water Resources Research*, *52*, 5301–5321. https://doi.org/10.1002/2015WR018056

Marzadri, A., Tonina, D., & Bellin, A. (2011). A semianalytical three-dimensional process-based model for hyporheic nitrogen dynamics in gravel bed rivers. *Water Resources Research*, *47*, W11518. https://doi.org/10.1029/2011wr010583

Marzadri, A., Tonina, D., & Bellin, A. (2012). Morphodynamic controls on redox conditions and on nitrogen dynamics within the hyporheic zone: Application to gravel bed rivers with alternate-bar morphology. *Journal of Geophysical Research*, *117*, G00N10. https://doi.org/10.1029/2012jg001966

Marzadri, A., Tonina, D., & Bellin, A. (2013). Quantifying the importance of daily stream water temperature fluctuations on the hyporheic thermal regime: Implication for dissolved oxygen dynamics. *Journal of Hydrology*, *507*, 241–248. https://doi.org/10.1016/j.jhydrol.2013.10.030

Monsen, N. E., Cloern, J. E., Lucas, L. V., & Monismith, S. G. (2002). A comment on the use of flushing time, residence time, and age as transport time scales. *Limnology and Oceanography*, *47*(5), 1545–1553. https://doi.org/10.4319/lo.2002.47.5.1545

Packman, A. I., & Brooks, N. H. (2001). Hyporheic exchange of solutes and colloids with moving bed forms. *Water Resources Research*, *37*(10), 2591–2605. https://doi.org/10.1029/2001WR000477

Peterson, B. J., Wollheim, W. M., Mulholland, P. J., Webster, J. R., Meyer, J. L., Tank, J. L., et al. (2001). Control of nitrogen export from watersheds by headwater streams. *Science*, *292*(5514), 86–90. https://doi.org/10.1126/science.1056874

Precht, E., Franke, U., Polerecky, L., & Huettel, M. (2004). Oxygen dynamics in permeable sediments with wave-driven pore water exchange. *Limnology and Oceanography*, *49*(3), 693–705. https://doi.org/10.4319/lo.2004.49.3.0693

Raudkivi, A. J. (1997). Ripples on stream bed. *Journal of Hydraulic Engineering*, *123*(1), 58–64. https://doi.org/10.1061/(ASCE)0733-9429

Roley, S. S., Tank, J. L., & Williams, M. A. (2012). Hydrologic connectivity increases denitrification in the hyporheic zone and restored floodplains of an agricultural stream. *Journal of Geophysical Research*, *117*, G00N04. https://doi.org/10.1029/2012JG001950

Rutherford, J., Latimer, G., & Smith, R. (1993). Bedform mobility and benthic oxygen uptake. *Water Research*, *27*(10), 1545–1558. https://doi.org/10.1016/0043-1354(93)90099-4

Sawyer, A. H. (2015). Enhanced removal of groundwater-borne nitrate in heterogeneous aquatic sediments. *Geophysical Research Letters*, *42*, 403–410. https://doi.org/10.1002/2014GL062234

Sawyer, A. H., & Cardenas, M. B. (2009). Hyporheic flow and residence time distributions in heterogeneous cross-bedded sediment. *Water Resources Research*, *45*, W08406. https://doi.org/10.1029/2008WR007632

Schmadel, N. M., Ward, A. S., Lowry, C. S., & Malzone, J. M. (2016). Hyporheic exchange controlled by dynamic hydrologic boundary conditions. *Geophysical Research Letters*, *43*, 4408–4417. https://doi.org/10.1002/2016GL068286

Soulsby, R. L., & Whitehouse, R. J. S. (1997). Threshold of sediment motion in coastal environments. In *Pacific Coasts and Ports '97, Christchurch, New Zealand, September 7–11, 1997: Proceedings of the 13th Australasian Coastal and Ocean Engineering Conference and the 6th Australasian Port and Harbour Conference*, (Vol. 1, pp. 145–154). Christchurch: University of Canterbury

Trauth, N., Schmidt, C., Vieweg, M., Maier, U., & Fleckenstein, J. H. (2014). Hyporheic transport and biogeochemical reactions in pool-riffle systems under varying ambient groundwater flow conditions. *Journal of Geophysical Research: Biogeosciences*, *119*, 910–928. https://doi.org/10.1002/2013JG002586

Triska, F. K., Jackman, A. P., Duff, J. H., & Avanzino, R. J. (1994). Ammonium sorption to channel and riparian sediments: A transient storagepool for dissolved inorganic nitrogen. *Biogeochemistry*, *26*(2), 67–83. https://doi.org/10.1007/BF02182880

van Rijn, L. C. (1984a). Sediment transport: Part I—Bed load transport. *Journal of Hydraulic Engineering*, *110*(12), 1733–1754. https://doi.org/10.1061/(ASCE)0733-9429

van Rijn, L. C. (1984b). Sediment transport: Part III—Bed forms and alluvial roughness. *Journal of Hydraulic Engineering*, *110*(10), 1431–1456. https://doi.org/10.1061/(ASCE)07339429

van Rijn, L. C. (1993). *Principles of sediment transport in rivers, estuaries and coastal seas*, *Aqua publications*. Amsterdam, the Netherlands: Aqua Publications.

Venditti, J. G., Church, M., & Bennett, S. J. (2005). Morphodynamics of small-scale superimposed sand waves over migrating dune bed forms. *Water Resources Research*, *41*, W10423. https://doi.org/10.1029/2004WR003461

Wörman, A., Packman, A. I., Marklund, L., Harvey, J. W., & Stone, S. H. (2007). Fractal topography and subsurface water flows from fluvial bedforms to the continental shield. *Water Resources Research*, *34*, L07402. https://doi.org/10.1029/2007GL029426

Zarnetske, J. P., Haggerty, R., Wondzell, S. M., Bokil, V. A., & González-Pinzón, R. (2012). Coupled transport and reaction kinetics control the nitrate source-sink function of hyporheic zones. *Water Resources Research*, *48*, G11508. https://doi.org/10.1029/2012wr011894

Zarnetske, R., Haggerty, S., Wondzell, M., & Baker, M. A. (2011). Dynamics of nitrate production and removal as a function of residence time in the hyporheic zone. *Journal of Geophysical Research*, *116*, G01025. https://doi.org/10.1029/2010JG001356

Zheng, L., Cardenas, M. B., & Wang, L. (2016). Temperature effects on nitrogen cycling and nitrate removal-production efficiency in bed form-induced hyporheic zones. *Journal of Geophysical Research: Biogeosciences*, *121*, 1086–1103. https://doi.org/10.1002/2015JG003162

Zlotnik, V. A., Toundykov, D., & Cardenas, M. B. (2015). An analytical approach for flow analysis in aquifers with spatially varying top boundary. *Groundwater*, *53*, 335–341. https://doi.org/10.1111/gwat.12205